Estimation of ship dynamics with a multi-platform radar imaging system

Fabrizio Santi, Debora Pastina, Marta Bucciarelli

***Abstract*—Distributed ISAR exploits the data acquired by multiple radar sensors carried by multiple platforms working in formation to increase the cross range resolution with respect to the value achievable by single platform systems. In this frame, the paper addresses the problem of the estimation of the ship dynamics, i.e. yaw, pitch and roll rotation motions, exploiting the signals collected by such multi-platform radar imaging systems providing angular diversity in order to enable the focusing of the distributed ISAR images. Specifically, in this work a multi-angle formation of sensors is considered and the corresponding Maximum Likelihood estimator and Cramer Rao Bound are derived. Then, a new Doppler matching based technique is proposed as a sub-optimal approach exploiting only the linear component of the phase of the received signals. The performance analysis proves the effectiveness of the proposed techniques to separately estimate the horizontal, radial and vertical components of the rotation vector, therefore making possible both the focusing and accurate cross-range scaling of the distributed ISAR products (as well as of the low resolution ISAR images regarding the different sensors) and, as a further advantage, providing knowledge of the orientation of the corresponding image projection planes. The analysis of experimental multi-sensor datasets confirms the feasibility of the proposed techniques.**

***Index Terms*— radar imaging, Inverse SAR (ISAR), multiplatform, multistatic, motion estimation.**

I. INTRODUCTION

THE monitoring and protection of the maritime environment is a challenging issue since a great variety of human activities usually takes place in the maritime scenario. The traditional legal civil/military maritime traffic/activities must be added to the irregular traffic, which can be responsible for illegal actions such as smuggling, illegal fishing, illegal dumping of pollutants and irregular migration. At the same time, the typical scenario for search and rescue operations is the maritime scenario. In the context outlined above the analysis of features/signatures of ship targets is of fundamental importance and radar imagery can be used for this purpose. As known, all-weather all-day radar images of moving targets can be obtained by exploiting the Inverse Synthetic Aperture Radar (ISAR) principle: wide bandwidth waveforms are transmitted to achieve fine range resolution while cross-range resolution is obtained on the basis of the synthetic aperture provided by the motion of the target itself, [1]-[2]. Thus, ISAR products can enable the classification of non-cooperative targets (i.e. ships not equipped with the Automatic Identification System, AIS) and can support search and rescue operations for both cooperative and non-cooperative targets. Obviously, the quality of these products strictly depends on the particular target motion conditions. Specifically ISAR assumes the sensor nearly stationary and the ship to be imaged rotating with respect to its center, being the rotation described by the effective rotation rate vector, [1]-[2]. Different kinds of images can be achieved depending on the different orientations of such vector, namely the 3D structure of the target is projected on a 2D Image Projection Plane (IPP) depending on the specific target rotation motion and radar acquisition geometry, [1]-[2]. Moreover, the cross range resolution is always determined by the aperture of the angle of view, and since the complex motion can strongly limit the usable Coherent Processing Interval (CPI), in many situations a poor cross-range resolution is obtained. These circumstances can have negative impact on the quality of the achievable ISAR images and therefore on the performance of NCTR (Non Cooperative Target Recognition) procedures, [3]-[4], usually fed with ISAR images, [5]-[9]. The use of multiple sensors/channels (MS) systems observing the same target and the joint exploitation of the acquired data seem to be a viable solution to overcome the above limitations and to improve the performance with respect to conventional single sensor/channel (SS) ISAR systems. Indeed, in the recent literature the exploitation of MS systems for target imaging purposes has received considerable attention: in particular it has been considered mainly for i) 3D target reconstruction and ii) target imaging with enhanced quality.

With specific reference to 3D target reconstruction, Interferometric ISAR (InISAR) relies on the use of multiple antennas properly located on the same platform and connected to separate channels. The exploitation of the interferometric phases measured at the available baselines allows the estimate of the height of the imaged target scatterers with respect to the IPP thus enabling 3D reconstruction. Different interferometric approaches have been proposed from first contributions, [10]-[14], to more recent ones as [15] using MIMO techniques jointly with sparse signal recovery and [16] using two orthogonal baselines combined with a CLEAN approach.

With the aim to provide ISAR products with enhanced quality with respect to the conventional SS case, the distributed ISAR (DISAR) concept was introduced in [17]-[19]. It consists in the exploitation of the data acquired by multiple radar sensors carried by multiple platforms working in formation to increase the cross range resolution with respect to the value achievable by single platform systems. As additional advantages of the distributed system, it is worth to mention also its robustness to failures and systems reconfiguration capability. Similarly to [17]-[19], in [20] multiple observations are coherently combined to reduce the CPI required to achieve a given cross-range resolution. Spatial diversity has been considered also in [21] for improving the 2D (range&cross-range) resolution cell. Obviously, in both cases (increase of resolution/reduction of required CPI) the focusing of these DISAR images requires the knowledge of the target rotation motion typically a priori unknown. In this frame, the focus of this paper is on the exploitation of the signals acquired by such multiple sensors for ship 3D rotation motion estimation: this enables the enhanced imaging, at the same time overcoming limitations usually experienced by SS estimation techniques.

The ship complex motion, resulting from the interaction of the object with the sea surface, is typically described as the superimposition of a translation and a rotation around vertical, lateral and longitudinal axes, defined as the yaw, pitch and roll motions, respectively, [22]. Many techniques can be found in literature exploiting SS data to perform the estimation of the target rotational motion. Usually, SS techniques aim at estimating only the factor needed for cross-range scaling (i.e. the effective rotation rate) and can be roughly categorized in three kinds. The first group comprises the image quality-based methods that estimate the scale parameter depending on target rotation as that value providing the best image quality [23]-[25]. The second group exploits series of range-Doppler (RD) images achieved by dividing the whole observation time in sub-apertures, [26]-[30]. Finally, the third group obtains the motion information by extracting the high-order terms of the phase of some prominent point scatterers (PPS) [31]-[34]. These techniques usually assume that the rotational motion of the target is confined to a 2D plane during the coherent processing interval (CPI), and they can experience significant losses when this assumption is not verified and the target develops 3D motion, [35]. Moreover, even in presence of 2D motion, the achievement of good accuracy can impose severe constraints on target size, signal to background ratio and used CPI, [32]. To cope with the above-mentioned problems/limitations, knowledge based approach has been proposed in [36]. Such a technique works for ship targets exploiting some *a priori* information regarding the ship silhouette; however, despite the restriction to a specific kind of target, the estimation of the horizontal component is subordinate to observe the target with particular acquisition geometries. It makes sense that the exploitation of data acquired by multiple sensors providing spatial diversity could help in extracting the information concerning the 3D motion needed for DISAR images formation (as explained above).

Few contributions can be found in literature concerning the use of MS ISAR data acquired from geometrically distributed systems for autofocus (translation motion compensation) and rotation motion estimation. Particularly an entropy based multistatic autofocus technique has been proposed in [37] while, with specific regard to rotation motion estimation, in [38]-[40] formations of sensors with different aspect angles have been considered for the estimation of motion of targets undergoing rotations mainly around a vertical axis. In this paper, we consider a formation of sensors with proper aspect and grazing diversity and we exploit the acquired data to provide the estimates of the three components of the rotation vector, therefore enabling the focusing and cross-range scaling of the DISAR images and, as a further advantage, the estimation of the IPP orientation. To this purpose, two different MS techniques are proposed using both model based and model free approaches. Exploiting the phase history of selected dominant scatterers, a Maximum Likelihood (ML) technique is first derived for the estimation of the full rotation vector (some preliminary results along this line were previously reported in [41]). Then a sub-optimum technique is derived which does not require any specific assumption on the phase model and exploits the Doppler positioning of the selected scatterers (Doppler-matching DM based technique). The study of the theoretical performance by means of the evaluation of the Cramer Rao Bound (CRB) and the simulated performance analysis are shown, demonstrating the capability of the proposed approach at providing high accuracy in the estimation of the rotation vector components and highlighting the robustness of the Doppler matching based technique. Finally, in order to validate the proposed techniques, results obtained by applying them to experimental MS ISAR data acquired in anechoic chamber are also shown.

The paper is organized as follows: in Section II the MS system geometry and the echo model are introduced; in Section III the proposed MS estimation techniques are presented, and their performance are analyzed in Section IV under ideal and non-ideal conditions; Section V shows the results achieved against experimental MS data sets, and Section VI concludes the paper. Analytical details are reported in the appendices.

II. MULTI-SENSOR ISAR GEOMETRY AND ECHO MODEL

The considered scenario consists in a set of $N \geq 3$ platforms carrying a sensor, characterized by either transmitting or receiving, or both transmitting and receiving capabilities, observing a moving ship. Hereinafter, we consider the special case of a single platform equipped with an active sensor (sensor 0), while the remaining $N-1$ carry receiving only devices. To be noticed that the concept could be easily generalized to combinations of active and passive sensors. In the inertial reference system (O,x,y,z) north-west-up with origin in the position the target fulcrum occupies at aperture centre, the nth sensor belonging to the formation is characterized by its distance D_n from the origin, its aspect angle ζ_n, measured clockwise starting from y-axis, and its grazing angle ψ_n, see Fig. 1.

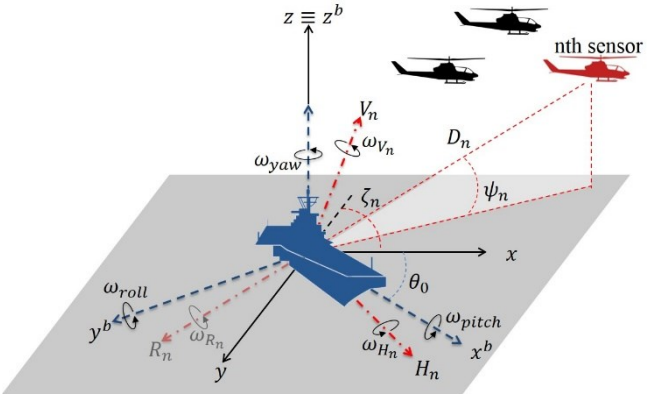

Fig. 1. Multi-sensor acquisition geometry.

The target is modeled as a rigid body in the far field with K dominant scatterers, with complex reflectivity constant during the time aperture T_a. As usual in ISAR literature, the target motion is decomposed as the translation of a reference point and the rotation of the body around that point. As previously stated, we assume any relative translational motion between the platforms and the target already compensated, i.e. the platforms and the target fulcrum can be considered stationary. The focus is therefore on the target rotation, which is usually described by the yaw, pitch and roll motions defined as the rotation around the vertical, lateral and longitudinal axis of the target, respectively, described by the rotation vector $\boldsymbol{\omega}_{RPY} = [\omega_{roll} \quad \omega_{pitch} \quad \omega_{yaw}]^T$. In the body reference system (O, x^b, y^b, z^b), defined as integral with the target and with origin in the target fulcrum, the kth scatterer is located in $\boldsymbol{p}_k = [x_k^b \quad y_k^b \quad z_k^b]^T$ and its rotation is described by the rotation vector $\boldsymbol{\omega}_{RPY}$. For sake of simplicity, we assume that the change between the body reference system and (O, x, y, z) is given by only a clockwise rotation of an angle θ_0 around the z-axis, being θ_0 the initial heading angle of the target, so that $z_b \equiv z$.

The echo model is here given in the range compressed (fast time) & slow time domain, with reference to K prominent target scatterers observed by the N sensors and extracted by following the procedure detailed in Section III.A. The signal received by sensor n ($n = 0, \dots, N-1$) from the kth scatterer at time t is written as

$$g_{k,n}(t) = \xi_{k,n} \cdot s_{k,n}(t) + \eta_{k,n}(t) \tag{1}$$

where $\xi_{k,n} = A_{k,n} \cdot e^{j\varphi_{k,n}}$ is the unknown but deterministic complex reflectivity as viewed by the nth sensor, $\eta_{k,n}$ is the zero-mean Gaussian distributed complex background contribution with power σ_η^2 and $s_{k,n}(t)$ is the normalized scatterer echo written as

$$s_{k,n}(t) = exp\left\{-j\frac{2\pi}{\lambda}[r_{k,0}(t) + r_{k,n}(t)]\right\} = exp\{-j\phi_{k,n}(t)\} \tag{2}$$

where $r_{k,n}(t)$ is the distance of the kth scatterer of the target from the nth sensor in the formation and λ the wavelength.

Above equations imply that range migration related to rotation motion can be neglected: this assumption can be regarded as reasonable due to the short CPI here considered to focus the N low resolution images. In any case, if range migration occurs, an iterative procedure could be followed to cope with it, [42].

Considering that in the time aperture T_a the radars collect M slow time samples at instants t_m $\left(m = -\frac{M}{2}, \dots, \frac{M}{2} - 1\right)$ with sampling frequency equal to the Pulse Repetition Frequency (PRF), the joint probability density function associated to each sample of the data collected by the nth sensor for the kth scatterer is

$$f\left(g_{k,n}(m)\right) = \frac{1}{\pi\sigma_\eta^2} exp\left\{-\frac{|g_{k,n}(m) - \xi_{k,n} \cdot s_{k,n}(m)|^2}{\sigma_\eta^2}\right\} \tag{3}$$

Therefore, under the hypothesis of independent noise samples $\eta_{k,n}(t_m)$, the joint probability density function of the collected data pertaining to the K scatterers can be written as

$$\begin{aligned} f(\boldsymbol{g}) &= \prod_{m=1}^{M}\prod_{n=1}^{N}\prod_{k=1}^{K} f\left(g_{k,n}(t_m)\right) = \\ &= \frac{1}{\pi^{KNM}\sigma_\eta^{2 \cdot KNM}} exp\left\{-\frac{\sum_{m=1}^{M}\sum_{n=1}^{N}\sum_{k=1}^{K}|g_{k,n}(t_m) - \xi_{k,n} \cdot s_{k,n}(t_m)|^2}{\sigma_\eta^2}\right\} = \\ &= \frac{1}{\pi^{KNM}\sigma_\eta^{2 \cdot KNM}} exp\left\{-\frac{1}{\sigma_\eta^2}(\boldsymbol{g} - \boldsymbol{S\Xi})^\dagger(\boldsymbol{g} - \boldsymbol{S\Xi})\right\} \end{aligned} \tag{4}$$

where $\boldsymbol{g} = [\boldsymbol{g}_1^T \quad \boldsymbol{g}_2^T \quad \dots \quad \boldsymbol{g}_K^T]^T$ is the $KNM \times 1$ data vector collecting the acquired signals with $\boldsymbol{g}_k = \left[\boldsymbol{g}_{k,0}^T \quad \dots \quad \boldsymbol{g}_{k,N-1}^T\right]^T$ and $\boldsymbol{g}_{k,n} = \left[g_{k,n}(t_{-M/2}) \quad \dots \quad g_{k,n}(t_{M/2-1})\right]^T$, $\boldsymbol{\Xi} = [\boldsymbol{\Xi}_1 \quad \dots \quad \boldsymbol{\Xi}_K]^T$ is the $KN \times 1$ complex amplitude vector with $\boldsymbol{\Xi}_k = [\xi_{k,0} \quad \dots \quad \xi_{k,N-1}]$ and $\boldsymbol{S} = diag(\boldsymbol{S}_1 \quad \dots \quad \boldsymbol{S}_K)$ is the $KNM \times KN$ diagonal block phase matrix, where the kth $NM \times N$ block is a diagonal block matrix $\boldsymbol{S}_k = diag(s_{k,1} \quad \cdots \quad s_{k,N})$ and $\boldsymbol{s}_{k,n} = [e^{j\phi_{k,n}(t_{-M/2})} \quad \dots \quad e^{j\phi_{k,n}(t_{M/2-1})}]^T$ is the $M \times 1$ block; † is the hermitian operator.

To completely specify the model here presented, it is useful to develop the expression of the distance $r_{k,n}(t)$ as a function of the target rotation. To the purpose, the local (O, H_n, R_n, V_n) reference system [36], representing the point of view of each platform belonging to the formation as sketched in Fig. 1, is introduced. The r_n-axis ($\hat{\boldsymbol{r}}_n$ unit vector) is the nth Line Of Sight (LOS) direction, the h_n-axis is given by the unit vector $\hat{\boldsymbol{h}}_n$ normal to $\hat{\boldsymbol{r}}_n$ and belonging the (x,y) plane and the v_n-axis is given by the unit vector $\hat{\boldsymbol{v}}_n$ normal to the (R_n, H_n) plane. We point out that in the following analysis the (O, H_0, R_0, V_0) reference system pertaining to the active sensor in the formation will act as the global reference system: indeed the estimation procedures devised in the present paper will allow retrieving the component of the target rotation motion vector $\boldsymbol{\omega} = [\omega_H \; \omega_R \; \omega_V]^T = \boldsymbol{\omega}_0$ as defined in this global reference system.

At aperture centre $t_0 = 0$ the transformation from body reference system to (O, H_n, R_n, V_n) for sensor n can be expressed by means of the matrixes $\boldsymbol{M}_{\psi_n}$ and $\boldsymbol{M}_{\zeta_n}$, which describe respectively an anticlockwise rotation of the absolute reference system around the x-axis with the grazing angle ψ_n and a clockwise rotation around the z-axis with the aspect angle ζ_n:

$$\boldsymbol{q}_{k,n}^0 = \begin{bmatrix} h_{k,n}^0 & r_{k,n}^0 & v_{k,n}^0 \end{bmatrix}^T = \boldsymbol{M}_{\psi_n}\boldsymbol{M}_{\zeta_n}\boldsymbol{M}_{\theta}\boldsymbol{p}_k \quad (5)$$

being $\boldsymbol{M}_{\theta}$ the rotation matrix accounting for the initial heading angle of the target. Because of the 3D rotation motion for a rolling, pitching, and yawing target, we can assume that the scatterer in $\boldsymbol{q}_{k,n}^0$ rotates around the radial, horizontal and vertical axis (as viewed by the nth sensor). Let $\vartheta_{\gamma}^n(t)$ be the angle, changing with time, swept around the γ_n-axis ($\gamma = H, R, V$); therefore, we have

$$\begin{bmatrix} h_{k,n}(t) \\ r_{k,n}(t) \\ v_{k,n}(t) \end{bmatrix} = \begin{bmatrix} C_{\vartheta_V^n}C_{\vartheta_R^n} & \left(S_{\vartheta_V^n}C_{\vartheta_H^n} + C_{\vartheta_V^n}S_{\vartheta_R^n}S_{\vartheta_H^n}\right) & \left(S_{\vartheta_V^n}S_{\vartheta_H^n} - C_{\vartheta_V^n}S_{\vartheta_R^n}C_{\vartheta_H^n}\right) \\ -S_{\vartheta_V^n}C_{\vartheta_R^n} & \left(C_{\vartheta_V^n}C_{\vartheta_H^n} - S_{\vartheta_V^n}S_{\vartheta_R^n}S_{\vartheta_H^n}\right) & \left(C_{\vartheta_V^n}S_{\vartheta_H^n} + S_{\vartheta_V^n}S_{\vartheta_R^n}C_{\vartheta_H^n}\right) \\ S_{\vartheta_R^n} & -C_{\vartheta_R^n}S_{\vartheta_H^n} & C_{\vartheta_R^n}C_{\vartheta_H^n} \end{bmatrix} \cdot \boldsymbol{q}_{k,n}^0 \quad (6)$$

being $S_x = sin\left(x(t)\right)$ and $C_x = cos\left(x(t)\right)$.

The expression of the distance $r_{k,n}(t)$ in (2) can be found from (6), but further mathematics is needed to properly explicit its dependence on the target rotation motion $\boldsymbol{\omega}$. A first step is to expand $C_{\vartheta_{\gamma}^n}$ and $S_{\vartheta_{\gamma}^n}$ in (6) in Taylor series at second order around t_0, in the hypothesis of uniform rotations, i.e. $\vartheta_{\gamma}^n(t) = \omega_{\gamma_n} t$; the vector $\boldsymbol{\omega}_n = \begin{bmatrix} \omega_{H_n} & \omega_{R_n} & \omega_{V_n} \end{bmatrix}^T$ can be achieved by applying the same rotation matrices in (5) to the vector $\boldsymbol{\omega}_{RPY}$. The expression of the distance $r_{k,n}(t)$ becomes

$$r_{k,n}(t) = -h_{k,n}^0\omega_{V_n}t + r_{k,n}^0\left(1 - \frac{\omega_{H_n}^2 t^2}{2} - \frac{\omega_{V_n}^2 t^2}{2}\right) + v_{k,n}^0\left(\omega_{H_n}t + \omega_{V_n}\omega_{R_n}t^2\right),\ -\frac{T_a}{2} \le t \le \frac{T_a}{2} \quad (7)$$

Writing the components of $\boldsymbol{\omega}_n$ as a function of the rotation motion as viewed in the global reference system (O, H_0, R_0, V_0) according to the transformation matrix $\boldsymbol{U}_{n\to 0} = \boldsymbol{M}_{\psi_0}\boldsymbol{M}_{\zeta_0}\boldsymbol{M}_{\zeta_n}^{-1}\boldsymbol{M}_{\psi_n}^{-1}$, from (2) and (7) it is possible to explicit the dependence of the phase of the signal backscattered from the kth scatterer and received by the nth sensor on the vector $\boldsymbol{\omega}$

$$\phi_{k,n}(t) = \frac{2\pi}{\lambda}\left[r_{k,0}(t) + r_{k,n}(t)\right] = \frac{2\pi}{\lambda}\left[r_{k,0}^0 + r_{k,n}^0 + \lambda f_{d_{k,n}}(\boldsymbol{\omega})t + \beta_{k,n}(\boldsymbol{\omega})t^2\right] \quad (8)$$

where $f_{d_{k,n}}(\boldsymbol{\omega})$ is the scatterer Doppler frequency at the image time t_0 and $\beta_{k,n}(\boldsymbol{\omega})$ is the focus parameter

$$f_{d_{k,n}}(\boldsymbol{\omega}) = \frac{1}{\lambda}\sum_{\gamma=h,R,V} a_{k,n}^{\gamma}\left(\psi_0, \psi_n, \zeta_0, \zeta_n, \boldsymbol{q}_{k,n}^0\right)\omega_{\gamma}$$
$$\beta_{k,n}(\boldsymbol{\omega}) = \sum_{\gamma=\mathrm{H,R,V}}\sum_{\delta=\mathrm{H,R,V}} b_{k,n}^{\gamma\delta}\left(\psi_0, \psi_n, \zeta_0, \zeta_n, \boldsymbol{q}_{k,n}^0\right)\omega_{\gamma}\omega_{\delta} \quad (9)$$

It is necessary to underline that coefficients $a_{k,n}^{\gamma}$ and $b_{k,n}^{\gamma\delta}$ depend on the sensor positions through the aspect and grazing angles $(\psi_0, \psi_n, \zeta_0, \zeta_n)$ as well as on the scatterer coordinates at t_0, $\boldsymbol{q}_{k,n}^0$. It is supposed that the latter can be retrieved with a certain approximation by the range measures collected at the different sensors in the formation, i.e. $\boldsymbol{q}_{k,n}^0 = \boldsymbol{q}_{k,n}^0\left(r_{k,n}^0\right)$, as explained in the following (see section IIIA, equation (10)). Therefore, once the position vector $\boldsymbol{q}_{k,n}^0$ has been retrieved, according to the known acquisition geometry, the $a_{k,n}^{\gamma}$ and $b_{k,n}^{\gamma\delta}$ coefficients could be deterministically computed.

III. MULTI-SENSOR ESTIMATION TECHNIQUES

In this section, the proposed MS rotation motion estimation techniques are described. A requirement for the techniques to properly work is the capability of correctly associating brightest spots in the N images as corresponding to the same scatterer of the target. How to achieve this result is described in the following subsection IIIA. Once this step is accomplished, the exploitation of both linear and quadratic phase terms of the model in (8) leads to the derivation of the ML technique described in subsection IIIB. Finally, subsection IIIC shows how a suboptimum DM technique can be devised based on the extraction of the Doppler frequencies of the selected scatterers in the different available images (namely by exploiting the linear component of the phase) and explains how such suboptimum technique is more insensitive to possible signal model mismatch. In both cases (ML and DM) it will be proven how the proper exploitation of the information acquired in spatial diversity allows us to estimate the full 3D rotational motion of the target, namely not only the horizontal and vertical components but also the radial one, which usually cannot be estimated by SS techniques.

A. Extraction and association of the dominant scatterers

The proposed MS techniques are based on the assumption that the same target scatterers can be selected in the N images formed by processing the N acquired signals. Many automatic methods have been proposed in the past for the extraction of the position of the PPS, [43], [44]. The pre-processing aimed at correctly extracting and associating the PPS is composed by three steps, namely images formation, scatterers extraction and scatterers association as described in the following.

1. Images formation: for each sensor the corresponding RD image is focused by Fourier transforming the range compressed&slow-time data with respect to slow-time. Thus, N RD images are obtained.
2. Scatterers extraction: a procedure based on image segmentation is applied to each image in order to detect and separate the dominant target scatterers. As in [36], this procedure first applies a proper threshold to the RD image in order to identify the positions characterized by high energy level; then rejects those detected regions constituted by few pixels; finally returns the scatterers positions by applying a 2D peak detection algorithm to the cleaned image coming from the previous step.
3. Scatterers association relies on the assumption that the same scatterer is observed in the N exploited acquisitions. It has to be remarked that the proposed techniques apply to

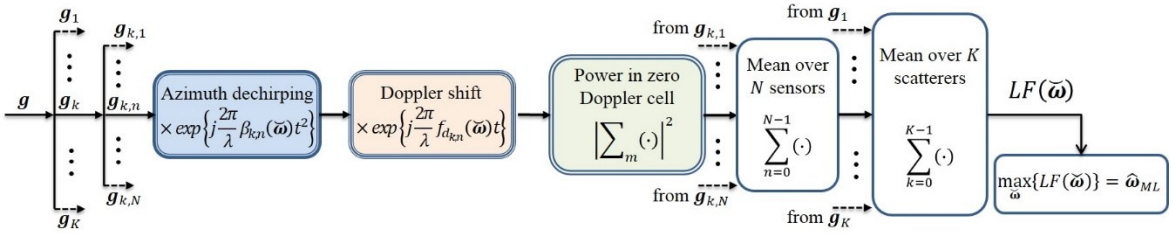

Fig. 2. Maximum Likelihood based processing scheme.

operative scenarios implying quite limited changes of the observation angle over the different acquisitions so that the target can be assumed in the pseudo-monostatic region (angular differences lower than about 5 degrees), [45]. However, it is well known that ISAR images are generally quite sensitive to changes of target orientation with respect to the radar LOS, and scatterers' distribution may vary even for limited angular separations (due to the susceptibility of coherent imaging to target scintillation). Nevertheless, it has been demonstrated that in ISAR imaging some scatterers persist over a certain degree of illumination angle [46], and many techniques relying on those scatterers have been successfully employed in autofocus and NCTR procedures [47]. Bright points that can be associated with single-scatterer scattering centres are less sensitive to variation of the radar perspective, and therefore are suitable for the subsequent estimation process. Useful techniques to discriminate among spots deriving from single/multiple point sources have been proposed [9], however, a full discussion about this topic is beyond the scope of this paper. Furthermore, the proposed estimation techniques need only extracting a limited number of such scatterers. Given the simplified conditions of small illumination angle changes and the need of few points, the strategy suggested here is selecting few isolated scatterers at the edges of the target in all the N images, such as the bow scatterer of a ship or the tail of an aircraft. In such conditions, the simple nearest neighboring method, as in [44], can be adopted to associate the scatterers in the different IPPs.

Hereafter, we assume that K scatterers have been properly associated in the different images. The range bins corresponding to these scatterers are extracted from data in range compressed&slow-time domain, and Doppler filtering is applied in order to discard the contribution of other minor scatterers and clutter background in the same range bin.

At this point, the data vector $\boldsymbol{g}$ with the statistic in (4) is obtained and the coordinates of the selected scatterers can be retrieved by the range measures collected at the different sensors in the formation. In particular, the relation between the measured slant ranges and the scatterer positions in (5) is given by

$$\boldsymbol{q}_{k,n}^{0} = \boldsymbol{M}_{\psi_n}\boldsymbol{M}_{\zeta_n}\boldsymbol{R}^{\ddagger}\boldsymbol{r}_k \tag{10}$$

In the above equation, $\boldsymbol{r}_k$ denotes the $N \times 1$ vector collecting the measured slant ranges $\frac{r_{k,n}^{0}+r_{k,0}^{0}}{2}$. $\boldsymbol{R}$ is an $N \times 3$ matrix, which depends on the geometric distribution of the multi-platform radar system, transforming the scatterer coordinates in the $(0, x, y, z)$ reference system in the measured ranges, and its nth row is given by $\left[-\frac{S_{\zeta_n}C_{\psi_n}+S_{\zeta_0}C_{\psi_0}}{2} \quad \frac{C_{\zeta_n}C_{\psi_n}+C_{\zeta_0}C_{\psi_0}}{2} \quad -\frac{S_{\psi_n}+S_{\psi_0}}{2}\right]$. Finally, ‡ indicates the pseudo-inverse operator. It is worth to notice that in the proposed MS formation we consider a joint multi-aspect/multi-grazing formation of $N \geq 3$ sensors: therefore the linear system (10) is characterized by a good degree of stability, and the scatterer coordinates can be recovered even in presence of errors due to imprecision in the knowledge of the sensors positions and the quantization of the slant range axis. Therefore, we can consider as known the $a_{k,n}^{\gamma}$ and $b_{k,n}^{\gamma,\delta}$ parameters in (9).

B. Maximum likelihood estimator

Based on the statistical model of the data in (4), it could be shown (see Appendix A), that the Maximum Likelihood estimate of the rotation rate vector is given by

$$\hat{\boldsymbol{\omega}}_{ML} = arg\ \max_{\boldsymbol{\omega}}\{LF(\boldsymbol{\omega})\} = arg\ \max_{\boldsymbol{\omega}}\left\{\sum_{n=0}^{N-1}\sum_{k=1}^{K}\left|\boldsymbol{s}_{k,n}^{\dagger}\boldsymbol{g}_{k,n}\right|^2\right\} \tag{11}$$

where $LF(\boldsymbol{\omega})$ is the likelihood function.

As it is apparent from (11), for each selected scatterer and considered sensor the ML estimator performs a coherent processing of the data to accomplish the estimation task. Let $[\breve{\omega}_H, \breve{\omega}_R, \breve{\omega}_V] = \breve{\boldsymbol{\omega}}$ be the rotation rate vector under test: as depicted in Fig. 2, this coherent elaboration of the data consists of the compensation of the linear and quadratic terms of the phase in (8) as a function of $f_{d_{k,n}}(\breve{\boldsymbol{\omega}})$ and $\beta_{k,n}(\breve{\boldsymbol{\omega}})$. For the kth selected scatterer, the signal pertaining the nth sensor $\boldsymbol{g}_{k,n}$ is multiplied by $\exp\left\{j\frac{2\pi}{\lambda}\beta_{k,n}(\breve{\boldsymbol{\omega}})t^2\right\}$ and $\exp\left\{j\frac{2\pi}{\lambda}f_{d_{k,n}}(\breve{\boldsymbol{\omega}})t\right\}$. The former operation is an azimuth dechirping procedure, whereas the latter corresponds at introducing a shift in the Doppler domain equal to $f_{d_{k,n}}(\boldsymbol{\omega}) - f_{d_{k,n}}(\breve{\boldsymbol{\omega}})$. The following coherent summation of the slow time samples and squared modulus extraction allow extracting the power of the (focused and Doppler compensated) scatterer. The power values concerning the kth scatterer as observed by the N sensors data are then averaged. We point out that the output of the processing

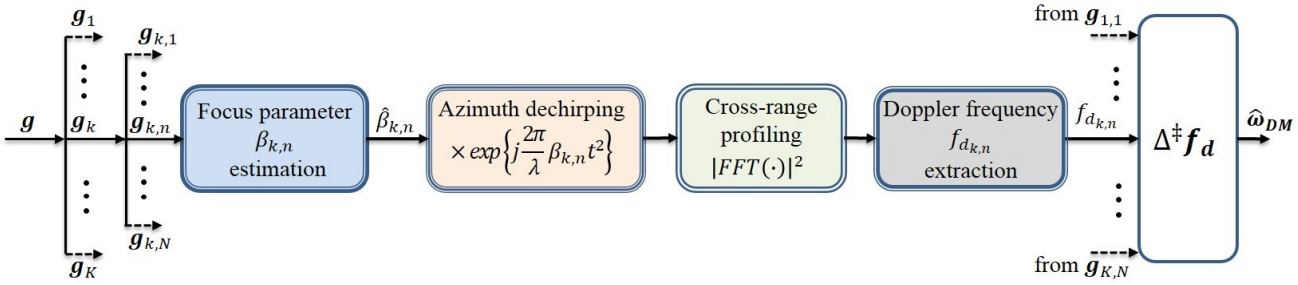

Fig. 3. Doppler matching based processing scheme.

of each signal vector $\boldsymbol{g}_k$ will be the highest when $\breve{\boldsymbol{\omega}} = \boldsymbol{\omega}$, namely when $\boldsymbol{s}_{k,n}^{\dagger} = \boldsymbol{s}_{k,n}^{\dagger}(\breve{\boldsymbol{\omega}})$ is matched to the signal under consideration. Such a processing is carried out for all the K selected scatterers, and the obtained power values are subsequently averaged, ultimately resulting in $LF(\breve{\boldsymbol{\omega}})$. The value $\breve{\boldsymbol{\omega}}$ corresponding to its global maxima is assumed as the estimated $\hat{\boldsymbol{\omega}}_{ML}$.

C. Doppler matching based technique

As well known, the ML estimator can reach the highest accuracy (CRB evaluated in the next section), but on the other hand it requires a maximization over a 3D space, which makes heavy the required computational load and moreover can be problematic when local maxima are present. Therefore, it is also interesting to derive sub-optimum techniques not requiring the application of optimization procedures. To this purpose, in this section we present a Doppler-matching (DM) based estimation technique to perform the motion estimation. Differently from the ML procedure, this technique exploits only the linear phase term in (8) to estimate the rotation vector $\boldsymbol{\omega}$.

The Doppler-matching based estimation technique processing scheme is depicted in Fig. 3. From each branch of the scheme, i.e. for each input signal vector $\boldsymbol{g}_{k,n}$, the processing aims at recovering the Doppler frequency of the scatterer $f_{d_{k,n}}$ and it is composed by the cascade of four steps: focusing parameter estimation, azimuth dechirping, cross-range profiling and Doppler frequency extraction.

The first step consists in the estimation of the best focusing parameter value for the selected range bin pertaining to the kth scatterer observed by the nth sensor. Differently from the ML technique such a step is not part of the rotation estimation searching procedure, but it is needed to remove Doppler migration before the subsequent processing. To this purpose the technique in [32] is exploited, which provides the best $\beta_{k,n}$ value regardless the components of $\boldsymbol{\omega}$. The estimated $\hat{\beta}_{k,n}$ is then used to compensate the Doppler spread (i.e. azimuth dechirping). Finally, the cross-range profile can be obtained by means of frequency analysis and the scatterer Doppler frequency can thus be extracted. By processing all the signal vectors $\boldsymbol{g}$, KN estimated Doppler frequencies are obtained.

Each Doppler frequency $f_{d_{k,n}}$ can be written as a linear combination of the rotation vector components ω_H, ω_R and ω_V with coefficients $a_{k,n}^{\gamma}$, (9). By considering all the N Doppler frequencies of each of the K selected scatterers, the following linear system can be written

$$\boldsymbol{\Delta\omega} = \boldsymbol{f_d} \tag{12}$$

where $\boldsymbol{\Delta} = \frac{1}{\lambda}[\boldsymbol{a}^{\mathrm{H}} \quad \boldsymbol{a}^{\mathrm{R}} \quad \boldsymbol{a}^{\mathrm{V}}]$ is the $[KN \times 3]$ matrix with $\boldsymbol{a}^{\gamma} = [\boldsymbol{a}_1^{\gamma} \quad \boldsymbol{a}_2^{\gamma} \quad \dots \quad \boldsymbol{a}_K^{\gamma}]^T$ and $\boldsymbol{a}_k^{\gamma} = [a_{k,0}^{\gamma} \quad \dots \quad a_{k,N-1}^{\gamma}]^T$, $\gamma = H, R, V$, and $\boldsymbol{f_d}$ is the vector of the KN measured Doppler frequencies. The estimated components of the rotation vector can be achieved by resorting to a least squares approach:

$$\hat{\boldsymbol{\omega}}_{\boldsymbol{DM}} = \boldsymbol{\Delta}^{\ddagger}\boldsymbol{f_d} \tag{13}$$

It could be shown that at least $K \geq 2$ scatterers are needed for the $\boldsymbol{\Delta}$ matrix to be full rank so that the full rotation rate vector can be retrieved; in contrast for the ML technique to work a single dominant scatterer could suffice (i.e. $K \geq 1$) since both linear and quadratic components of the scatterer phase are exploited.

The advantage of using the DM based technique with respect to the ML estimator is twofold. The first benefit depends on its model-free characteristic: indeed Doppler frequencies $f_{d_{k,n}}(\boldsymbol{\omega})$ are insensitive to potential angular accelerations, which would certainly affect the focus parameters $\beta_{k,n}(\boldsymbol{\omega})$ instead. Consequently, ML estimation performance would suffer from the mismatch between target motion model and actual dynamics, while DM technique would automatically adapt to the presence of not negligible angular accelerations. ML approach could definitely recover its performance if both angular velocity and acceleration were used to model the target motion to the expense of an increased the computational load, which is not a secondary issue. Indeed the second advantage of the DM estimation approach resides in its higher computational efficiency, if compared to the ML technique, since it does not require any optimization procedure to retrieve the estimated values, except for KN linear independent and parallelizable searches over the focus parameters. This represents a significant benefit with respect to the ML estimator, which requires the joint maximization over the 3D space of horizontal, radial and vertical uniform rotations (6D if accelerations are considered). Obviously, we expect the DM approach to provide lower estimation accuracy with respect to the theoretical performance,

met by the ML technique if the target motion is accurately modelled. Nevertheless, as discussed in the next section, such performance degradation is quite limited making the DM technique appealing for practical applications.

IV. Performance Analysis

A. Theoretical performance analysis

Considering the signal model in (4), the theoretical performance for the rotation motion estimation can be analyzed by evaluating the Cramer Rao lower Bound (CRB). It can be shown (see Appendix B) that the standard deviation of the estimation error for the γth component of the rotation vector (defined as $\delta\omega_\gamma = \widehat{\omega}_\gamma - \omega_\gamma$, being $\widehat{\omega}_\gamma$ and ω_γ the estimated and true value of ω_γ) for the model described above, is given by

$$CRB_{\omega_\gamma} = \sigma^2_{\omega_\gamma} = \frac{\lambda^2\sigma_\eta^2}{2\pi^2 MT_a^2}\frac{z_{\delta,\delta}z_{\mu,\mu}-z^2_{\delta,\mu}}{|\boldsymbol{Z}|}, \begin{cases} \gamma,\delta,\mu = H,R,V \\ \gamma\neq\mu,\delta\neq\gamma,\delta\neq\mu \end{cases} \quad (14)$$

being $\boldsymbol{Z}$ a 3×3 matrix whose element $z_{\gamma,\delta}$ $(\gamma,\delta = H,R,V)$ is given by the linear combination of two terms:

$$z_{\gamma,\delta} = \{L_{\gamma,\delta} + Q_{\gamma,\delta}(\boldsymbol{\omega})\} \quad (15)$$

The formers are related to the coefficients of the linear term of the phase in (9)

$$L_{\gamma,\delta} = \frac{1}{3}\sum_{n=0}^{N-1}\sum_{k=1}^{K} A^2_{k,n} a^\gamma_{k,n}\, a^\delta_{k,n} \quad (16)$$

whereas the latter are related to the coefficients of the quadratic term of the phase in (9)

$$Q_{\gamma,\delta}(\boldsymbol{\omega}) = \frac{T_a^2}{45}\sum_{n=0}^{N-1}\sum_{k=1}^{K} A^2_{k,n} \dot{b}^\gamma_{k,n}\dot{b}^\delta_{k,n} \quad (17)$$

with $\dot{b}^\gamma_{k,n}(\boldsymbol{\omega}) = {\partial\beta_{k,n}}/{\partial\omega_\gamma}$.

From the previous expressions, the case of the CRBs (14) with $Q_{\gamma,\delta} = 0$ (hereafter $CRB^L_{\omega_\gamma}$) is the maximum achievable accuracy when exploiting only the Doppler information but not the Doppler rate (as done by the Doppler-matching based technique), since it represents how the linear terms of the signal phases contribute to the estimation accuracy. On the other hand, the maximum accuracy we might achieve by exploiting only the quadratic term of the phases (as done in most of the SS estimation techniques, e.g. [25], [32], [33]) is represented by the CRBs (14) with $L_{\gamma,\delta} = 0$ (hereafter $CRB^Q_{\omega_\gamma}$). The maximum achievable accuracy for the ML estimator is obtained for both $L_{\gamma,\delta}, Q_{\gamma,\delta} \neq 0$ (hereafter CRB_{ω_γ}).

In order to study how the linear and quadratic terms of the phases affect the theoretical accuracy of the estimation, we compare $CRB^L_{\omega_\gamma}$, $CRB^Q_{\omega_\gamma}$ and CRB_{ω_γ}. For the analysis we consider the case of a ship target undergoing an angular motion given by $\omega_{roll} = 0.03$ rad/s , $\omega_{pitch} = 0.02$ rad/s, $\omega_{yaw} = -0.05$ rad/s. Without loss of generality, we assume the active radar sensor (reference sensor $n = 0$) observing the ship, having initial heading angle $\theta_0 = 0°$, with $\zeta_0 = \psi_0 = 0°$ (we

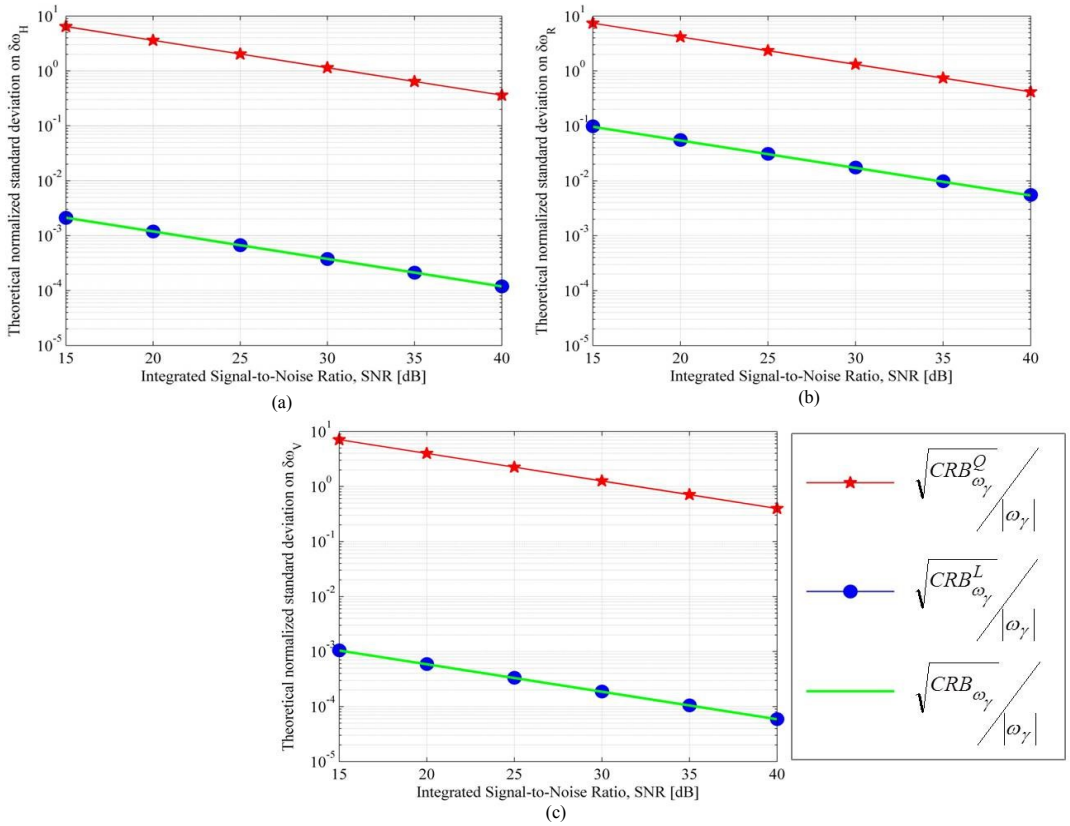

Fig. 4. Comparison of the theoretical accuracy achievable by exploiting the linear and/or the quadratic phase terms for the horizontal (a), radial (b) and vertical (c) components of the rotation vector.

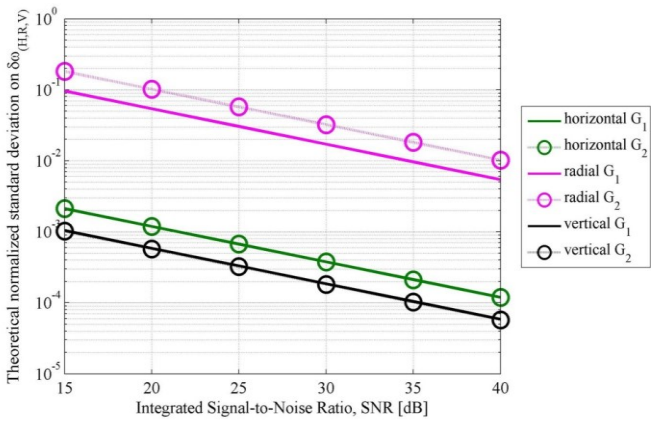

Fig. 5. Comparison of the theoretical accuracies achievable for different sensor displacements.

point out that in these specific conditions of observation, $x^b \equiv x \equiv h_0$, $y^b \equiv y \equiv r_0$, $z^b \equiv z \equiv z_0$, and therefore $\omega_{roll} \equiv \omega_H$, $\omega_{pitch} \equiv \omega_R$ and $\omega_{yaw} \equiv \omega_V$). The acquisition time is 0.5 sec, the wavelength is 3 cm and $D_0 = 30$ Km. Two additional platforms are considered carrying passive devices, having illumination angles equal to $\zeta_1 = -2°$, $\psi_1 = 1°$ and $\zeta_2 = 3°$, $\psi_2 = 5°$, and the mainmast and the bow scatterer, located in $\boldsymbol{p}_1 = [10, 0, 20]^T$m and $\boldsymbol{p}_2 = [30, 0, 0]^T$m, respectively, are selected.

Fig. 4 shows the theoretical normalized standard deviation of the estimation errors on the single components of the rotation vector as a function of the integrated signal-to-noise ratio, defined as $SNR_{k,n} = M\frac{A_{k,n}^2}{\sigma_\eta^2}$; here, for sake of simplicity, it is assumed to be independent from n and equal for both the scatterers. We can observe how the theoretical accuracy for the dechirping-based estimation is extremely poor; on the other hand, good performance can be achieved by the DM technique, reaching pretty much the same theoretical accuracy of the ML estimator.

It is worth to notice that dechirping-based techniques can reach a maximum theoretical accuracy depending on the angular motion value, since $CRB_{\omega_\gamma}^Q \equiv CRB_{\omega_\gamma}^Q(\boldsymbol{\omega})$, and therefore on the cross-range resolution. Consequently, dechirping-based estimations need longer CPI in order to increase the estimation accuracy, i.e. higher cross-range resolution, in case of slow rotating targets. Nevertheless, typically short CPIs are employed in ISAR imaging. In contrast, for a given SNR the theoretical accuracy of the DM technique depends only on system geometry and scatterers position (by means of $a_{k,n}^\gamma$ parameters), so that high quality estimations can be obtained for both fast and slow rotating targets.

It is also apparent how for all the SNR conditions the best performance is achieved for the vertical and horizontal components of the rotation vector, whereas the estimation of the radial component behaves slightly worse. However, it has to be underlined that, differently from the MS case, in a SS system it is not possible to estimate the radial rotation. Indeed the rotation around the radial axis does not affect the Doppler position of the scatterer. In contrast, in the MS formation case, both vertical and horizontal rotations $(\omega_{V_n}, \omega_{H_n})$ as locally viewed by each sensor in the formation can be represented as a function of all the components of the rotation vector $\boldsymbol{\omega}$. Therefore, the radial rotation can be estimated and recovered along with the vertical and horizontal components of the motion. Moreover, it is expected that the capability of the MS system to recover the radial rotation of the target improves if the angular separation among the sensors increases, since in such case a larger part of ω_R is projected onto the horizontal and vertical axes pertaining the nth sensor. In Fig. 5 the theoretical normalized standard deviation of the estimation errors on the horizontal, radial and vertical components of the rotation vector are compared when the estimation is performed by exploiting both the linear and quadratic terms of the phases for two different sensor displacements: in geometry 1 (G_1), the sensor displacement is as in Fig. 4, whereas in geometry 2 (G_2) we consider illumination angles being $\zeta_0 = \psi_0 = 0°$, $\zeta_1 = -1°$, $\psi_1 = 0.5°$, $\zeta_2 = 1.5°$, $\psi_2 = 2.5°$; remainder parameters are as in G_1. As expected, the wider angular diversity in G_1 resulted in an enhanced achievable accuracy of the radial rotation estimation than the one in G_2. In addition, one can observe negligible variations moving from G_1 to G_2 for the estimations concerning the horizontal and radial components. Therefore, from a theoretical point of view, even very small separations among the individual perspectives may provide high quality estimations of the horizontal and vertical rotations. Nevertheless, as it will be analysed ahead, a greater angular diversity greatly helps in the achievement of reliable estimations under non-ideal conditions.

B. Simulated performance analysis

The simulated scenario is given by a formation of three sensors comprising an active sensor ($n = 0$) transmitting in X-band ($\lambda = 3$ cm) and two additional receivers ($n = 1,2$). Without loss of generality, we consider an "L" shape formation, with the reference sensor 0 observing the target with $\zeta_0 = 0°$, $\psi_0 = 2°$ and $D_0 = 30$ Km, sensor 1 characterized by the same grazing angle as the active sensor but different aspect $\zeta_1 = 5°$ and, on the reverse, sensor 2 observing the target with the same aspect angle as the reference sensor but different grazing $\psi_2 = 7°$ ($D_1 \approx D_0 \approx D_2$). We consider the system observing a ship target of which the point model is given in Fig. 6. Ship dynamics consist in sinusoidal roll, pitch and yaw, namely the angles swept with time around the x_b, y_b and z_b axis are given by

$$\theta_\delta(t) = A_\delta \sin(2\pi f_\delta t + \phi_\delta) \tag{18}$$

A_δ, f_δ and ϕ_δ are the amplitude, the frequency and the initial phases of the sinusoidal rotations, respectively ($\delta = [\text{roll}, \text{pitch}, \text{yaw}]$). Table I lists the values considered for the simulations, along with the corresponding constant components of the motions $\omega_\delta = A_\delta 2\pi f_\delta \cos(\phi_\delta)$ and the accelerations $\dot{\omega}_\delta = -A_\delta(2\pi f_\delta)^2 \sin(\phi_\delta)$. Considering the initial heading angle $\theta_0 = 45°$ and the aperture time $T_a = 0.55$ s around the image time $t_0 = 0$ s, the three receivers provide the set of RD images shown in Fig. 7. As it is apparent, because of the limited separation among the radar perspectives, the three images are very similar, and the association of a large number of scatterers

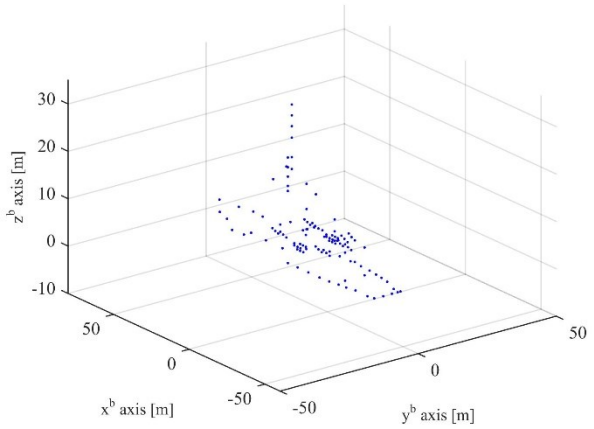

Fig. 6. Ship target model.

TABLE I. SIMULATED SHIP DYNAMICS

δ	A_δ [deg]	f_δ [Hz]	ϕ_δ [deg]	ω_δ [rad/s]	$\dot{\omega}_\delta$ [rad/s²]
yaw	1	0.2152	15	0.022	0.0077
pitch	1	0.1806	10	0.019	0.0038
roll	5	0.0930	12	0.049	0.0059

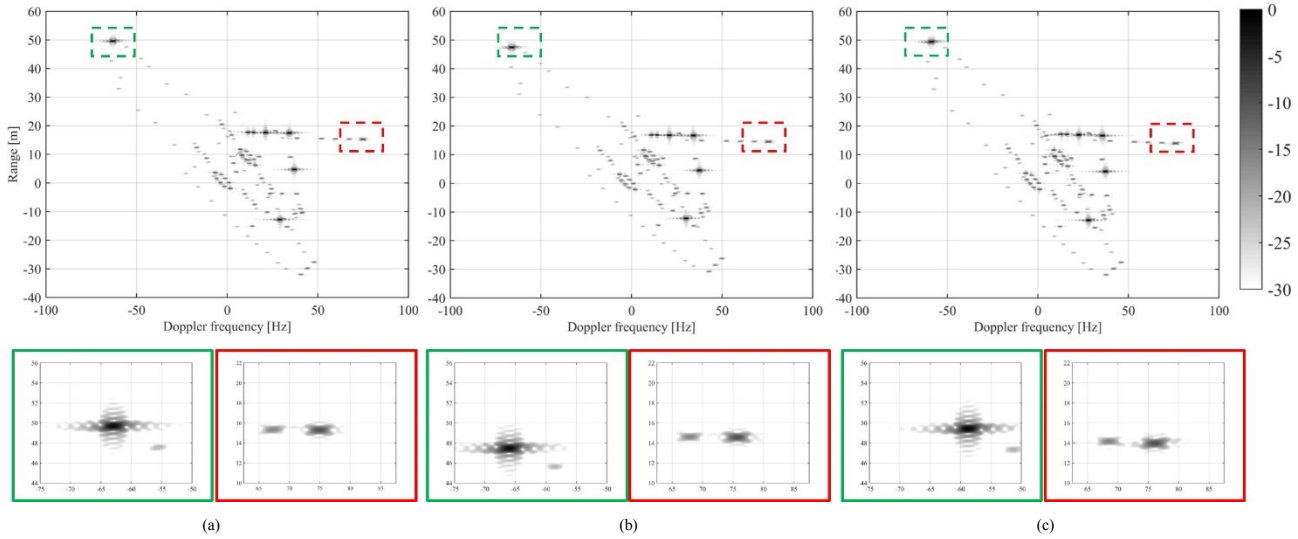

Fig. 7. Range-Doppler images of the ship target for sensor 0 (a), 1 (b) and 2 (c). Bottom boxes show the bow (green boxes) and mainmast (red boxes) scatterers, selected for the motion estimation process.

may be a not so difficult task. Obviously, as discussed in Section IIIA, in realistic scenarios only few prominent scatterers approximating the field from a point source can be extracted and associated in the multi-angle images. Therefore, for the subsequent analyses, we assume only $K = 2$ scatterers selected for the ship dynamics estimation; specifically, we assume that the bow and the mainmast scatterers, located in $\boldsymbol{p}_{\text{bow}} = [71.3, 0, 3.2]^T$m and $\boldsymbol{p}_{mast} = [23.4, 0, 23.3]^T$m in the body reference system, respectively, have been extracted from the three RD images.

Monte Carlo simulations have been carried out to evaluate the estimation performance as a function of the integrated SNR (10000 independent trials for each SNR value, assumed the same for both the selected scatterers and the same for the three RD images). In a first case study, we analyze the estimation performance when the ship undergoes uniform rotations during the aperture time. To this purpose, we consider the scenario in which the motion is only given by the constant components of the sinusoidal rotations in Table I. The red '×' and the blue 'o' markers in Fig. 8 represent the normalized standard deviation of the estimation error on the horizontal, radial and vertical components of the rotation vector achieved by the ML and the DM techniques, respectively, and the green full lines refer to the CRBs. As expected, the ML performance reaches the CRB for all the components of the rotation vector. Noticeably, the degradation of the performance achieved by applying the Doppler matching based techniques is extremely limited, as foreseen by the theoretical analysis in Fig. 4.

In a second case study, we assume the target interested by the full sinusoidal roll, pitch and yaw, and Fig. 9 shows the corresponding estimation results. We can observe that in such a case the DM technique outperforms the ML estimator, which shows a degradation of the performance due to the presence of not negligible accelerations in the rotation motions. Such degradations are due to the mismatching between the model considered to derive the ML estimator (i.e. constant rotation rate) and the simulated signal. In contrast, accelerations do not affect the performance of the Doppler matching based technique, thus it provides also in this case performance comparable with the CRB.

Previously we supposed the translation of the target

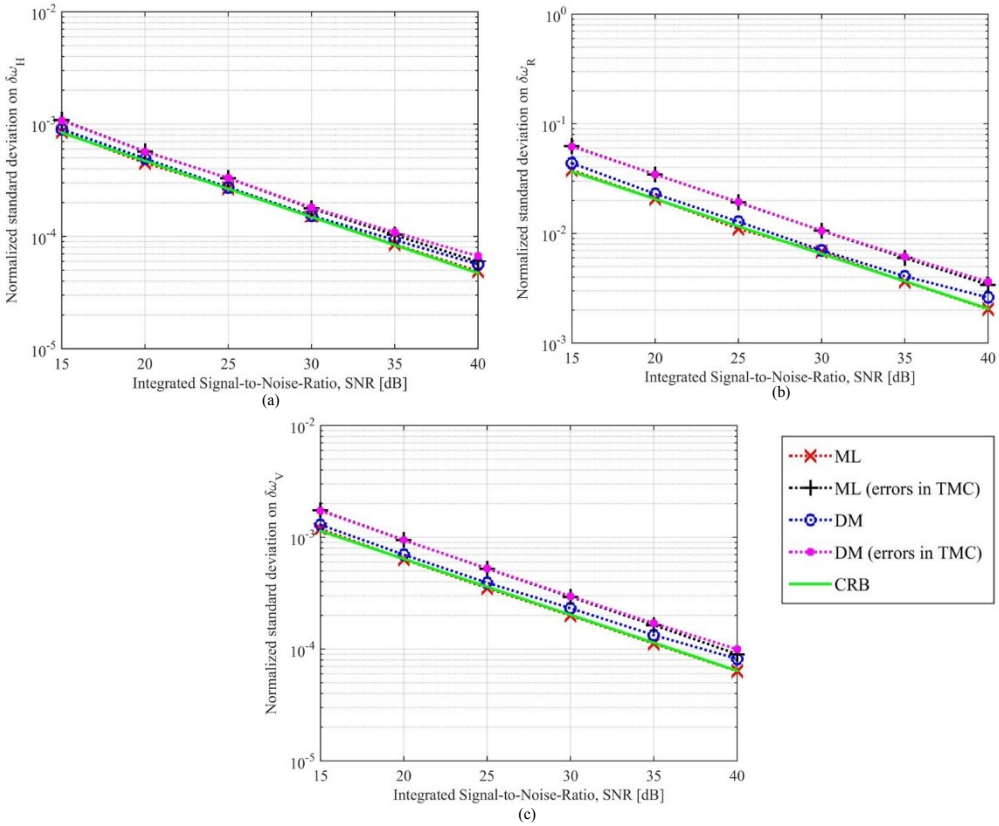

Fig. 8. Normalized standard deviation on the estimation error on the horizontal (a), radial (b) and vertical (c) components of the rotation vector in the case of uniform rotations – comparison for the ML, DM (without and with errors in TMC) and theoretical (CRB) performance.

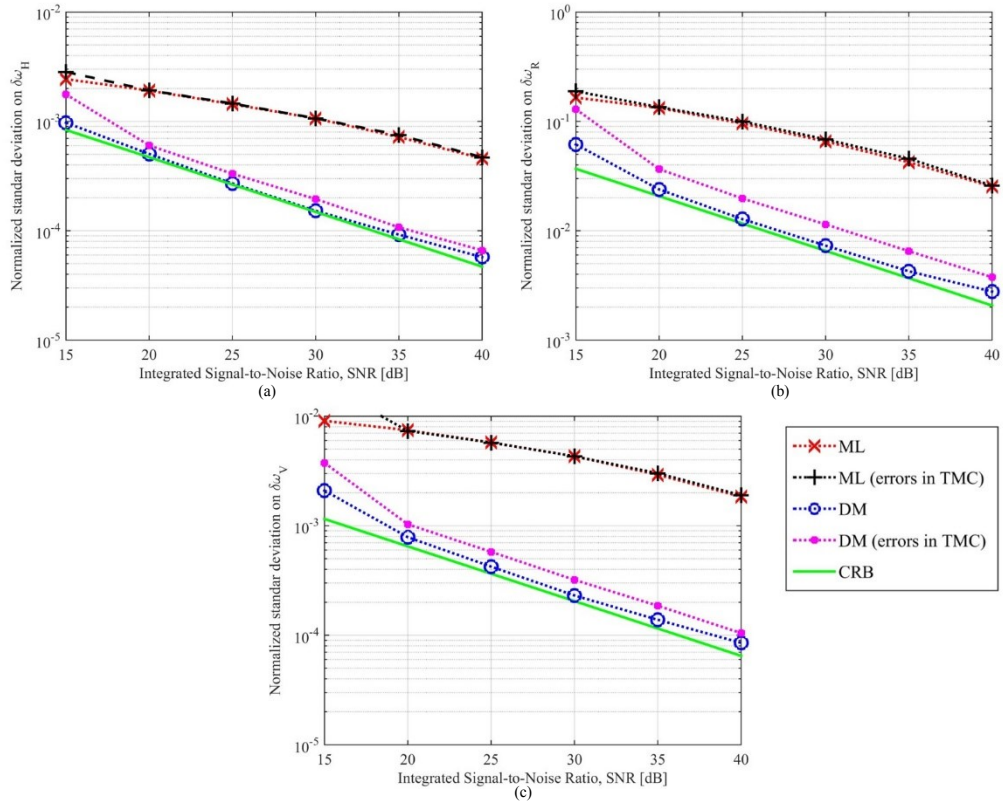

Fig. 9. Normalized standard deviation on the estimation error on the horizontal (a), radial (b) and vertical (c) components of the rotation vector in the case of sinusoidal rotations – comparison for the ML, DM (without and with errors in TMC) and theoretical (CRB) performance.

perfectly compensated following an ideal translational motion compensation (TMC) technique or autofocus procedure. In order to test the robustness of the proposed MS 3D rotational motion estimation approaches to non-ideal TMC, the following analyses have been performed. We simulate the outcome of the non-ideal TMC procedure as affected by linear and quadratic phase errors a_1 and a_2, respectively, both distributed according a zero mean Gaussian variable with standard deviations equal to the theoretical accuracy for the estimation of a constant amplitude polynomial phase signal embedded in AWGN, [48], namely $\sigma_{a_1} = \frac{\sqrt{6}}{SNR \cdot T_a}$ and $\sigma_{a_2} = \frac{\sqrt{90}}{(SNR \cdot T_a)^2}$. Black '+' and pink '.' markers in Fig. 8 and Fig. 9 show the normalized standard deviation of the estimation error of ML and DM techniques respectively as a function of the SNR when errors in the TMC are considered (10000 independent trials with independent errors for different sensors) for uniform and sinusoidal rotations. Looking at Fig. 8, it is apparent that for targets undergoing uniform rotations TMC phase errors slightly affect ML and DM techniques, providing the same accuracy levels as in the ideal case for 3 dB higher SNR. Moreover, it is apparent how both techniques show the same behavior with respect to the simulated phase errors. We would expect worse performance of the ML technique with respect to the DM approach, since in the latter case errors in the focusing parameter would be completely recovered in the 1D searching procedure prior the actual estimation stage. However, it has been demonstrated in Fig. 4 how even in the ML case the main contribution to the estimation is provided by the Doppler frequency diversity, as for the sub-optimal DM case. This explains why both techniques undergo nearly the same performance degradation in presence of both linear and quadratic TMC phase errors. For targets undergoing sinusoidal rotations, ML and DM techniques differentiate their behavior. Results in Fig. 9 confirm the trend that ML approach is worse since the model of the target motion is not compliant with the actual ship dynamic; moreover it is apparent how linear and quadratic TMC errors are surpassed by model errors, thus they don't further degrade the already deteriorated performance. On the other end, DM technique experiments the same level of performance degradation as in the uniform target motion case in Fig. 8, due to its robustness to model mismatch.

As stated in deriving the theoretical model, we assumed as ideally known the distances $\boldsymbol{r}_k$ of the kth scatterer from the N sensors and therefore we used the true positions $\boldsymbol{q}_{k,n}^0$ in (10) for the computation of the coefficients $a_{k,n}^\gamma$ and $b_{k,n}^\gamma$. However, in practical situations, the accuracy whereby the slant ranges of the scatterers are retrieved according the procedure IIIA is limited by the transmitted bandwidth, i.e. by the slant range resolution ρ_r, as well as by the SNR: therefore in this condition a performance degradation is expected. To analyse such effect we can assume the measured slant ranges vector $\boldsymbol{r}_k$ for the kth scatterer retrieved with an accuracy given by $\frac{c}{2}\frac{1}{B_G\sqrt{SNR}}$ being B_G the Gabor bandwidth, [49], and, as a consequence, the matrix $\boldsymbol{\Delta}$ in (12) perturbed by the errors in recovering the $a_{k,n}^H, a_{k,n}^R, a_{k,n}^V$ parameters. Fig. 10 shows the normalized standard deviation of the estimation errors obtained with the DM estimator. Fig. 10a shows the achieved estimation accuracy as a function of the slant range resolution for the same operative conditions in Fig. 8 and SNR = 30 dB. We can observe the reduction of the accuracy due the errors introduced in matrix $\boldsymbol{\Delta}$. However, even in these non-ideal conditions, very good performance can be achieved. Moreover, the robustness of the proposed MS system in estimating the rotation vector in the case of badly recovered scatterer slant ranges depends also on the sensor displacement. Indeed, the increasing of the angular diversities in both aspect and grazing makes the system (10) more stable (namely the matrix $\boldsymbol{R}$ is characterized by a lower condition number).

Fig. 10b shows the impact of the angular diversity on the estimation quality. In this case, we considered sensors 1 and 2 providing respectively aspect and grazing diversity Γ, namely $\zeta_1 = \zeta_0 + \Gamma$, $\zeta_2 = \zeta_0$, $\psi_1 = \psi_0$ and $\psi_2 = \psi_0 + \Gamma$; slant range resolution is set equal to 50 cm and SNR = 30 dB. As it is apparent, in the case of perturbed scatterers range coordinates, the increase of the angular diversity of the system enhances the quality of the estimations.

A further source of non-ideality is represented by possibly inaccuracies in the knowledge of the sensors positions. To analyze the technique robustness to the presence of deviations of the actual acquisition geometry from the nominal sensors

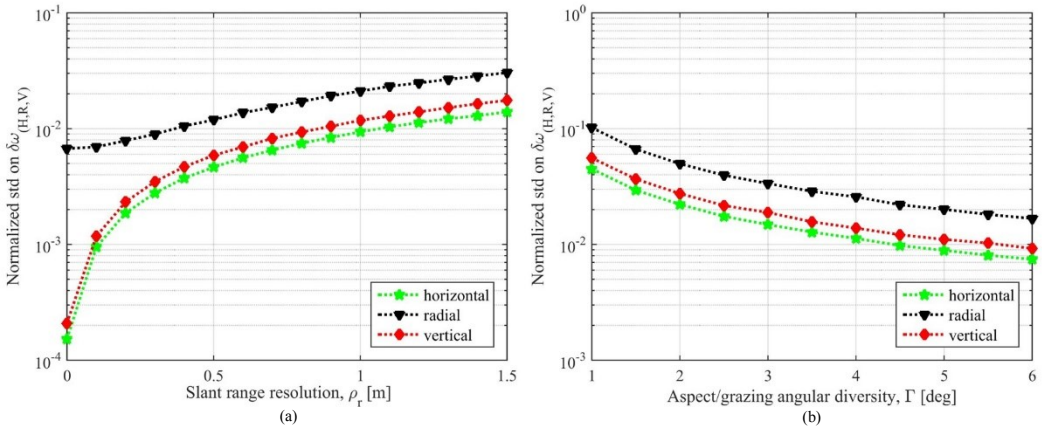

Fig. 10. DM based estimator performance for inaccurate knowledge of the slant range coordinates of the selected scatterers as a function of slant range resolution (a) and system geometry (b). SNR = 30 dB, $\psi_0 = 2°$, $D_0 = 30$ Km.

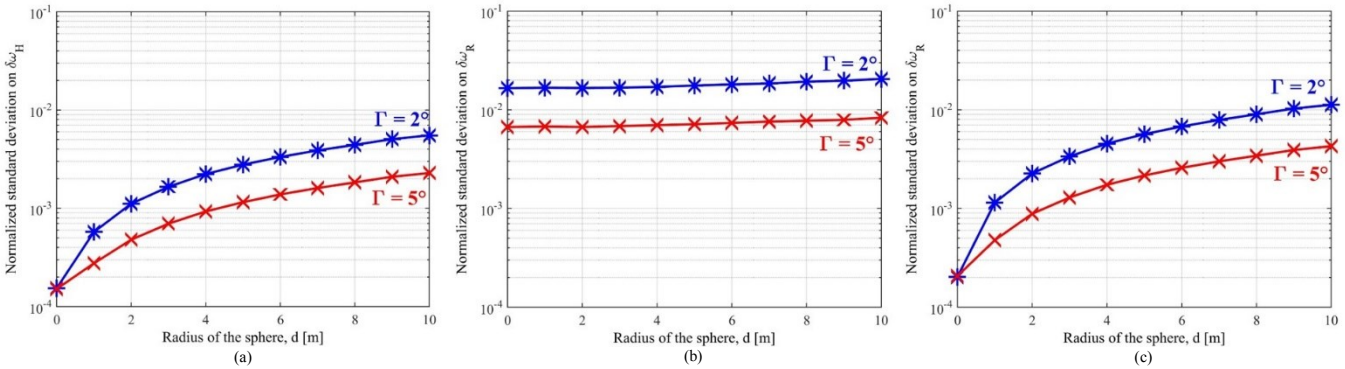

Fig. 11. Normalized standard deviation on the estimation error on the horizontal (a), radial (b) and vertical (c) components of the rotation vector obtained with the DM based estimator for deviation of the system geometry from the nominal displacement. SNR = 30 dB, $\psi_0 = 2°$, $D_0 = 30$ Km.

positions, we considered the position of each platform as a random variable uniformly distributed in a sphere, with center in the nominal position and radius d (different platforms are affected by independent errors). As in Fig. 10b, sensor 1 provides the aspect diversity and sensor 2 the grazing diversity, both equal to Γ. Fig. 11 shows the normalized standard deviation on the estimation errors on the three components of the rotation vector for different values of Γ as a function of d (10000 independent trials for each d value). As it is apparent, wider angular diversities allow the MS system to counteract the worsening of the estimation performance in the case of perturbation of the sensor positions. Nevertheless, we point out that even in the case of small angular separation among the sensors, very good performance can be obtained even in the case of medium/high deviation of the sensors from their nominal positions. Moreover, the worst case here considered of $d = 10$ m is a quite conservative assumption, since modern sensors can be equipped with high-precision satellite navigation receivers.

V. Application to Experimental Multi-Sensor ISAR Data

A. Experimental setup

MS ISAR data have been acquired in an anechoic chamber at the SELEX Galileo (now Finmeccanica) facility in Caselle (Turin, Italy). The measurements are based on the use of a Compact Range system, which generates a planar wave front in the test area; therefore, the hypothesis of target in far field applies. The system includes a parabolic reflector, a system of feeds and a proper positioning of the target under test. The antenna is an offset parabolic reflector P/N 5755 made by Scientific Atlanta. The reflector is illuminated by a spherical wave front from a transmitting feed located into its focus; the signal from the target is focalized into its focus where the receiving feed is located. The measurements instrumentation is based on a HP 8510C Network Analyzer. The system transmits a series of narrowband pulses in the Ku-band ($\lambda = 1.82$ cm), with the carrier frequency increased pulse by pulse by a fixed frequency step equal to 3.75 MHz to form a burst (stepped-frequency waveform). The overall spanned bandwidth is 3 GHz, resulting in $\rho_r = 5$ cm, and the angular step of the turntable burst to burst is $\delta\theta = 0.07°$. A second receiving feed has been added 60 cm apart from the transmitting one, thus resulting in a bistatic channel having aspect diversity $\Delta\zeta = 4.3°$ with respect to the monostatic link.

Two kinds of targets have been analyzed. The first one is a grid of metallic cylinders, emulating the case of isolated point scatterers; in a second experiment, an aircraft model (ATR 42) has been considered as representative of a complex target since unfortunately no model of ship targets was available. Optical pictures of the used targets are shown in Fig. 12.

B. Distributed ISAR images

Fig. 13 shows the ISAR images of the aircraft obtained by applying the focusing technique presented in [50]; specifically, Fig. 13a is the image resulting when an overall illumination angle equal to $\Theta = 4.3°$ is selected from the monostatic channel, whereas Fig. 13b is the DISAR image obtained by selecting an illumination angle equal to $2.15°$ from the monostatic and $2.15°$ from the bistatic channel, so that a distributed overall aspect angle equal to $4.3°$ is again obtained. We can observe the very good similarity between the two images, confirmed by the comparison of the cross-range cuts around the scatterer corresponding to the tail of the aircraft (Fig. 13c). This confirms the validity of the hypotheses of coherency of the scatterers echoes and of stability of the positions of the scattering centers in the case of limited angular separation (bistatic angle of the order of 5° so that the pseudo-monostatic assumption applies). Moreover, we point out that the coherency of the scatterer echoes among different images is not strictly required for the proposed estimation techniques.

C. Motion estimation

To apply the MS motion estimation techniques to these experimental data some preliminary considerations are in order. The proposed estimation techniques need a twofold diversity, in both aspect and grazing illumination angles. Actually, this experiment emulates a multi-aspect formation without grazing diversity. Consequently, some assumptions are mandatory. (i) We assume a flat target geometry, so that for each scatterer we have $\boldsymbol{p}_k = [x_k, y_k, 0]^T$; therefore, since $\psi_n = 0°$ for both the monostatic channel ($n = 0$) and the bistatic channel ($n = 1$), the vertical coordinate of every scatterer is null ($v_{k,n} = 0, k =$

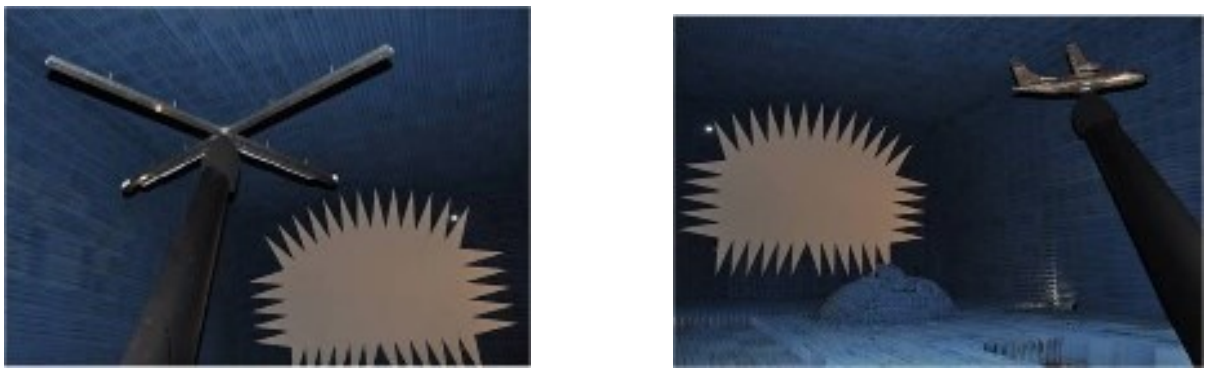

(a) (b)

Fig. 12. Experimental datasets – a) framework with grid of metallic cylinders and b) ATR42 aircraft model (1:20 scale).

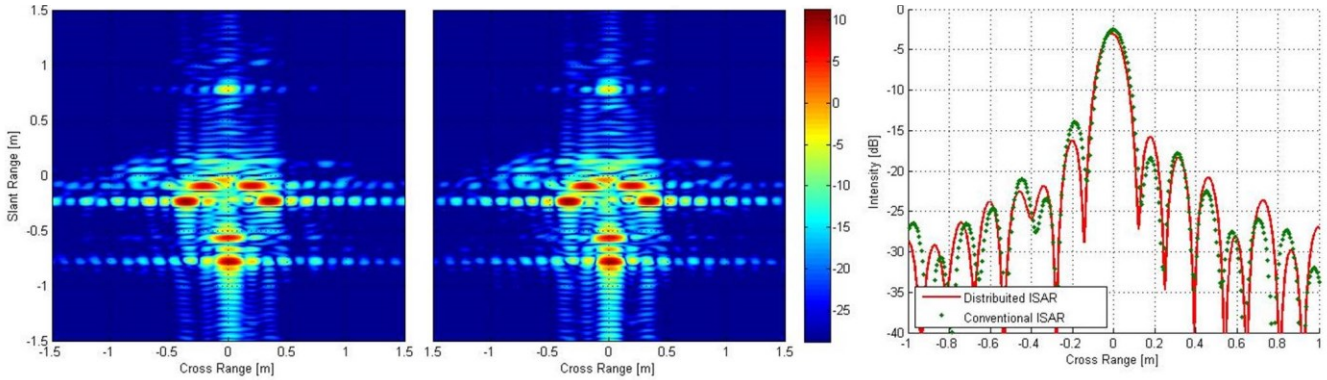

(a) (b) (c)

Fig. 13. ATR42 aircraft model images – (a) Conventional monostatic ISAR, (b) DISAR, (c) cross-range cut comparison.

$1,..,K$); as a consequence, $\boldsymbol{q}_{k,0}$ and $\boldsymbol{q}_{k,1}$ can be recovered despite the lack of diversity on the grazing angle domain. (ii) Moreover, we point out that the rotational motion produced by the turntable is a yaw motion, and we assume as known such information. In these particular conditions, the ML and Doppler matching based techniques properly modified are able to work.

Let $\delta\theta$ be the objective of the estimation. In order to built $LF(\delta\theta)$ each kth selected range bin concerning the nth receiving channel is multiplied by the exponential terms given by $exp\left\{j\frac{2\pi}{\lambda}(h_{k,0}+h_{k,n})m\widetilde{\delta\theta}\right\}$ and $exp\left\{j\frac{2\pi}{\lambda}(r_{k,0}+r_{k,n})m^2\widetilde{\delta\theta}^2\right\}$, corresponding to the Doppler shift and azimuth dechirping in Fig. 2, being $m=\left[-\frac{M}{2},\dots,+\frac{M}{2}-1\right]$ the burst index vector, M the number of considered bursts and $\widetilde{\delta\theta}$ the angular step under test. The value of $\widetilde{\delta\theta}$ which maximizes $LF(\delta\theta)$ is assumed as the ML estimation of the angular motion.

Regarding the Doppler matching based technique, we need to resolve the reduction of the linear system (12) given by

$$\boldsymbol{\Delta}_h\delta\theta=\boldsymbol{f}_\theta \tag{19}$$

being $\boldsymbol{\Delta}_h$ the column vector of matrix $\boldsymbol{\Delta}$ containing the $a_{k,n}^H$ entries and $\boldsymbol{f}_\theta$ the vector containing the angular frequency of the selected scatterers.

A further consideration concerns the impact of target size on the performance analysis. For the grid of metallic cylinders, the farthest cylinder from the fulcrum has distance equal to 1.45 m, whereas the aircraft model is about $[1.5\times 1]$ m^2. Due to the very limited size of the targets, a poor accuracy may be expected, since, as obvious, scatterers far away from the image center should be used to achieve good performance for rotation motion estimation. To counteract the problem of accuracy worsening caused by the limited target size we emulated a wider angular separation between the two receiving channels, considering different heading angles for the two (monostatic and bistatic) acquisitions. In such a way, the emulated aspect diversity between the two channels is $\widetilde{\Delta\zeta}=4.3°+\Delta\theta_0$, being $\Delta\theta_0$ the difference between the initial heading angles.

In a first case study, we considered the grid of metallic cylinders and initial heading angles $\theta_0=0°$ and $\theta_0=15°$. $M=38$ bursts were used for each channel to form the image, corresponding to a cross-range resolution $\rho_{cr}=20$ cm. Fig. 14 shows the resulting RD images. Despite the different illumination angles, the bright spots in the two images can be easily associated. The range bins in the monostatic and bistatic channels containing the bottom-right scatterer (white '×' in Fig. 14a,b) are selected to perform the estimation process, and the measured slant range values are exploited to recover the horizontal coordinates of the scatterer. The angular step-dependent likelihood function is built, Fig. 14c, and the tested $\delta\theta$ corresponding to its maximum is assumed as $\widehat{\delta\theta}_{ML}$, whereas the estimated $\widehat{\delta\theta}_{DM}$ is directly achieved from (19) starting from the measured $\boldsymbol{f}_\theta$. The results are reported in Table II and we

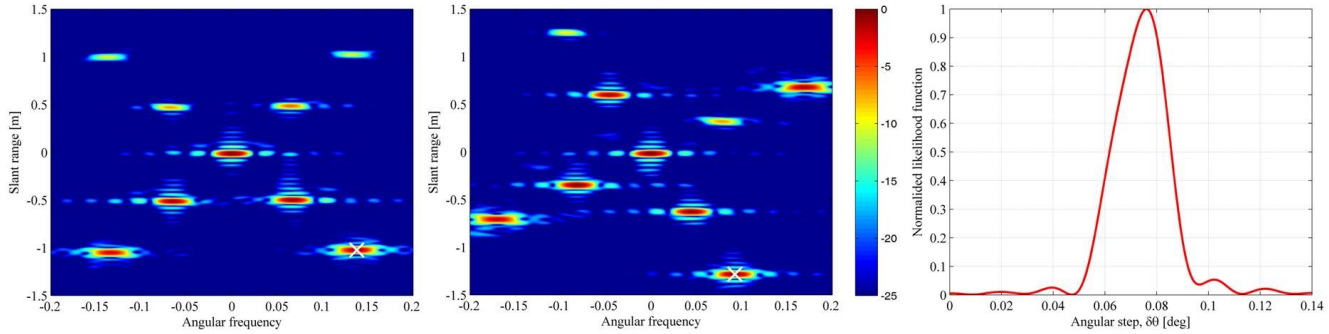

Fig. 14. Grid of metallic cylinders - Range Doppler images of (a) monostatic channel with $\theta_0 = 0°$, (b) bistatic channel with $\theta_0 = 15°$, and (c) likelihood function when the right bottom scatterer is selected.

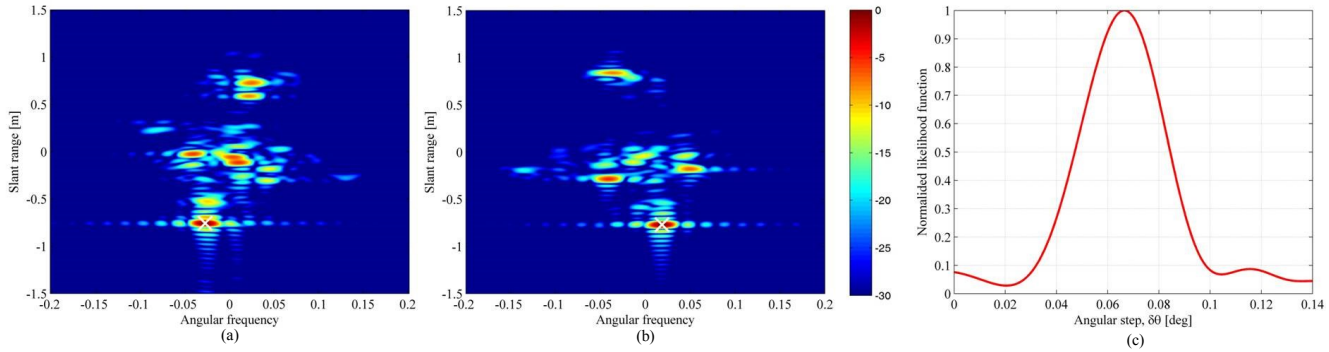

Fig. 15. ATR42 model - Range Doppler images of (a) monostatic channel with $\theta_0 = 15°$, (b) bistatic channel with $\theta_0 = -9°$, and (c) likelihood function when the nose scatterer is selected.

TABLE II. RESULTS FOR THE LIVE MULTI-SENSOR ISAR DATA

Target	Range-Doppler coordinates, monostatic channel	Range-Doppler coordinates, bistatic channel	Recovered horizontal positions, mono/bi-static channel	$\widehat{\delta\theta}_{ML}$ (normalized estimation error)	$\widehat{\delta\theta}_{DM}$ (normalized estimation error)
cylinders	-1.023 m, 0.139	-1.283 m, 0.093	0.960 m, 0.568 m	0.0714° (2.1%)	0.0707° (1.1%)
ATR42	-0.758 m, -0.028	-0.769 m, 0.018	-0.208 m, 0.163 m	0.0693° (1.0%)	0.0644° (8.0%)

can observe that both the techniques returned estimations close to the theoretical value.

In a second case study, we considered the aircraft model. For each channel, $M = 50$ bursts were used, resulting in $\rho_{cr} = 15$ cm, and the obtained RD images are shown in Fig. 15. Due to the smaller sizes of this target than the grid of metallic cylinders, a wider angular aperture than the previous case has been considered: heading angles were set to $\theta_0 = 15°$ and $\theta_0 = -9°$ for the monostatic and bistatic channels, respectively, therefore resulting in $\overline{\Delta\zeta} = 28.3°$. Such a value of angular separation is well beyond the operative bounds of the MS radar system we are considering in this work. However, even in such conditions we can identify more than one scatterer persisting in the two images, e.g. the cluster of four scatterers corresponding to the wings (the spots in the central region around $f_\theta \approx \pm 0.05$) and the nose of the aircraft. Because of the wings scatterers are too close to the target fulcrum, only the nose scatterer has been considered for the estimation (the selected points on the two RD images are highlighted with white '×' in Fig. 15). As for the previous case study, starting from the measured range-Doppler coordinates of the selected scatterer we are able to recover the estimated $\widehat{\delta\theta}_{DM}$, and by building LF (Fig. 15c) we can get its maximum as $\widehat{\delta\theta}_{ML}$. Table II collects the achieved results and, also for this case concerning a more complex target than the grid of metallic cylinders, both the techniques reached acceptable estimations.

We point out that the LF curve concerning the ATR42 model is larger than the curve pertaining to the grid of metallic cylinders, so that a greater standard deviation of the estimation error can be expected. Such a behavior follows from the selection of a scatterer closer to the target fulcrum, resulting in small variation of its position in different IPP. Scatterers sufficiently far from the target fulcrum should be selected to perform high quality estimations. Nevertheless, such a

condition is generally fulfilled in real cases, due to the greater size of real targets than the ones employed in the anechoic chamber and since the constraint of isolated scatterers requires the selection of scatterers on the edge of the targets. Shown results against experimental data further validate the effectiveness of the proposed approaches and support their practical application.

VI. Conclusions

The paper puts forward target motion estimation techniques for rolling, pitching and yawing ship by means of a multi-platform radar imaging system. The spatial diversity offered by the distributed system is exploited to retrieve the full 3D rotation rate vector (i.e. horizontal, vertical and radial components) thus enabling the multi-platform system to focus and scale ISAR images with resolution improved with respect to the single platform case and, as a further advantage, providing knowledge of the orientation of the corresponding image projection planes.

A Maximum Likelihood estimator has been derived, which exploits both the linear and quadratic terms of the phase of selected scatterers to achieve the best estimation accuracy. However, it requires a heavy computational load since it has to perform a 3D searching procedure over the rotation vector components, and, furthermore, it can show several shortcomings arising when the acquired data do not match the signal model. Therefore, a sub-optimal procedure has been devised and analytically described. This Doppler-matching based technique exploits only the linear term of the signal phase and it requires only parallel linear searching procedures, thus sensibly reducing the computational load. Moreover, it can achieve high performance, in line with the ML estimator that can be even outperformed if mismatching between the phase model and the received signal arise.

The performance of the techniques have been first analyzed at the theoretical level by means of the study of the CRB, and subsequently by means of simulations under different non-ideal conditions, showing the effectiveness of the techniques in estimating the ship motion.

Finally, the techniques have been tested against experimental multi-sensor datasets. As well as the case of a target composed by isolated point-like scatterers, the case of a complex target (an aircraft model was at our disposal) has been considered; the analysis proved that even for complex targets isolated scatterers can be associated in different projection planes, thus proving the feasibility of the proposed approaches.

Appendix

A. Analytical derivation of the Maximum Likelihood estimator

For the joint statistic in (4), the log-likelihood function is given by

$$ln\, f(\boldsymbol{g}) = -KNM\left(ln\,\pi + ln\,\sigma_\eta^2\right) - \frac{1}{\sigma_\eta^2}(\boldsymbol{g}-\boldsymbol{S\Xi})^\dagger(\boldsymbol{g}-\boldsymbol{S\Xi}) \tag{20}$$

Accounting for the hypothesis concerning the knowledge of the range-Doppler position of the target scattering centers, the unknown quantities in (20) are σ_η^2, $\boldsymbol{\Xi}$, $\boldsymbol{\omega}$. The ML estimator can be obtained as

$$\widehat{\boldsymbol{\omega}}_{ML} = argmax_{\boldsymbol{\omega}}\left\{argmax_{\sigma_\eta^2,\boldsymbol{\Xi}}[ln\, f(\boldsymbol{g})]\right\} \tag{21}$$

Let us consider first the maximization with respect to σ_η^2:

$$\frac{\partial\, ln\, f(\boldsymbol{g})}{\partial \sigma_\eta^2} = -\frac{KNM}{\sigma_\eta^2} + \frac{1}{\sigma_\eta^4}(\boldsymbol{g}-\boldsymbol{S\Xi})^\dagger(\boldsymbol{g}-\boldsymbol{S\Xi}) = 0$$
$$\Rightarrow \sigma_\eta^2 = \frac{(\boldsymbol{g}-\boldsymbol{S\Xi})^\dagger(\boldsymbol{g}-\boldsymbol{S\Xi})}{KNM} \tag{22}$$

By substituting in (21) we obtain

$$\widehat{\boldsymbol{\omega}}_{ML} = argmax_{\boldsymbol{\omega}}\left\{argmax_{\boldsymbol{\Xi}}\left[-KNM(\ln\pi+1) - KNM\ln\left(\frac{(\boldsymbol{g}-\boldsymbol{S\Xi})^\dagger(\boldsymbol{g}-\boldsymbol{S\Xi})}{KNM}\right)\right]\right\} \tag{23}$$

Let us consider the maximization with respect to $\boldsymbol{\Xi}$

$$\frac{\partial\left[-KNM(\ln\pi+1) - KNM\ln\left(\frac{(\boldsymbol{g}-\boldsymbol{S\Xi})^\dagger(\boldsymbol{g}-\boldsymbol{S\Xi})}{KNM}\right)\right]}{\partial\boldsymbol{\Xi}} = 2\boldsymbol{S}^\dagger\boldsymbol{g} - 2\boldsymbol{S}^\dagger\boldsymbol{S} =$$
$$0 \Rightarrow \boldsymbol{\Xi} = (\boldsymbol{S}^\dagger\boldsymbol{S})^{-1}\boldsymbol{S}^\dagger\boldsymbol{g} \tag{24}$$

By substituting in (23) we obtain

$$\widehat{\boldsymbol{\omega}}_{ML} = argmax_{\boldsymbol{\omega}}\left\{-KNM(\ln\pi+1) - KNM\ln\left[\frac{1}{KNM}\left|(\boldsymbol{I}-\boldsymbol{S}(\boldsymbol{S}^\dagger\boldsymbol{S})^{-1}\boldsymbol{S}^\dagger)\boldsymbol{g}\right|^2\right]\right\} = argmin_{\boldsymbol{\omega}}\left\{\left|(\boldsymbol{I}-\boldsymbol{S}(\boldsymbol{S}^\dagger\boldsymbol{S})^{-1}\boldsymbol{S}^\dagger)\boldsymbol{g}\right|^2\right\} \tag{25}$$

being $\boldsymbol{I}$ the $[KNM \times KNM]$ identity matrix. Based on (25), the ML estimate of the rotation rate vector is the $\boldsymbol{\omega}$ value which minimizes the power of the projection of the received signal into the subspace orthogonal to the useful signal. This corresponds to maximize the power of the projection of the received signal into the useful signal subspace, since $\left|(\boldsymbol{I}-\boldsymbol{S}(\boldsymbol{S}^\dagger\boldsymbol{S})^{-1}\boldsymbol{S}^\dagger)\boldsymbol{g}\right|^2 = \left|(\boldsymbol{I}-\boldsymbol{SLL}^\dagger\boldsymbol{S}^\dagger)\boldsymbol{g}\right|^2 = \boldsymbol{g}^\dagger\boldsymbol{g} - \boldsymbol{g}^\dagger\boldsymbol{S}(\boldsymbol{S}^\dagger\boldsymbol{S})^{-1}\boldsymbol{S}^\dagger\boldsymbol{g}$, where $\boldsymbol{L}$ is the matrix defined as $\boldsymbol{LL}^\dagger = (\boldsymbol{S}^\dagger\boldsymbol{S})^{-1}$. By substituting in (25), after simple manipulations we obtain the ML estimator as in (11).

B. Analytical derivation of the Cramer Rao Bound

In this appendix, we derive the CRB for the estimations of the three components of the rotation vector. Hereafter, $\gamma, \delta = H, R, V$; $k, u = 1, \dots, K$; $n, l = 0, \dots, N-1$. $Re\{\cdot\}$ and $Im\{\cdot\}$ denote the real and imaginary part operators, respectively.

The CRB can be evaluated via the Fisher information matrix $\boldsymbol{F}$, defined as in [51]

$$[\boldsymbol{F}]_{i,j} = E\left\{\frac{\partial\, ln\, f(\boldsymbol{g})}{\partial x_i}\frac{\partial\, ln\, f(\boldsymbol{g})}{\partial x_j}\right\} \tag{26}$$

being $E\{\cdot\}$ the mean operator and (x_i, x_j) any pair of the $2KN+4$ unknown parameters, i.e., the noise power σ_η^2, the KN modulus and the KN phases of the reflectivity of the K

scatterers and the horizontal, radial and vertical components of the rotation vector $\boldsymbol{\omega}$. The partial derivatives needed to evaluate (26) are

$$\frac{\partial \ln f(\boldsymbol{g})}{\partial \sigma_\eta^2} = -\frac{KNM}{\sigma_\eta^2} + \frac{1}{{\sigma_\eta^2}^2}\sum_{n=0}^{N-1}\sum_{k=1}^{K}\sum_{m=-M/2}^{M/2-1}\left|g_{k,n}(t_m) - A_{k,n}e^{-j[\varphi_{k,n}+\phi_{k,n}(t_m)]}\right|^2$$

$$\frac{\partial \ln f(\boldsymbol{g})}{\partial A_{k,n}} = \frac{2}{\sigma_\eta^2}\sum_{m=-M/2}^{M/2-1} Re\left\{g_{k,n}(t_m)e^{-j[\varphi_{k,n}+\phi_{k,n}(t_m)]} - A_{k,n}\right\} \quad (27)$$

$$\frac{\partial \ln f(\boldsymbol{g})}{\partial \varphi_{k,n}} = \frac{2}{\sigma_\eta^2}\sum_{m=-M/2}^{M/2-1} A_{k,n} Im\left\{g_{k,n}(t_m)e^{-j[\varphi_{k,n}+\phi_{k,n}(t_m)]}\right\}$$

$$\frac{\partial \ln f(\boldsymbol{g})}{\partial \omega_\gamma} = -\frac{4\pi}{\lambda\sigma_\eta^2}\sum_{n=0}^{N-1}\sum_{k=1}^{K}\sum_{m=-M/2}^{M/2-1} A_{k,n}\left(a_{k,n}^{\gamma}t_m + \dot{b}_{k,n}^{\gamma}t_m^2\right) Im\left\{g_{k,n}(t_m)e^{-j[\varphi_{k,n}+\phi_{k,n}(t_m)]}\right\}$$

$\boldsymbol{F}$ can be arranged in the following sixteen blocks:

$$\boldsymbol{F}_{1,1} = E\left\{\frac{\partial(\cdot)}{\partial\omega_\gamma}\frac{\partial(\cdot)}{\partial\omega_\delta}\right\} = \frac{2\pi^2 MT_a^2}{\lambda^2\sigma_\eta^2}\sum_{n=0}^{N-1}\sum_{k=1}^{K}\left(\frac{a_{k,n}^{\gamma}a_{k,n}^{\delta}}{3} + \frac{\dot{b}_{k,n}^{\gamma}\dot{b}_{k,n}^{\delta}}{20}T_a^2\right), \quad [3\times 3]$$

$$\boldsymbol{F}_{2,2} = E\left\{\frac{\partial(\cdot)}{\partial\varphi_{k,n}}\frac{\partial(\cdot)}{\partial\varphi_{u,l}}\right\} = \begin{cases}\frac{2M}{\sigma_\eta^2}A_{k,n}^2, (k,n)=(u,l)\\ 0 \quad\quad, (k,n)\neq(u,l)\end{cases}, \quad [KN\times KN]$$

$$\boldsymbol{F}_{3,3} = E\left\{\frac{\partial(\cdot)}{\partial A_{k,n}}\frac{\partial(\cdot)}{\partial A_{u,l}}\right\} = \begin{cases}\frac{2M}{\sigma_\eta^2}, (k,n)=(u,l)\\ 0 \quad, (k,n)\neq(u,l)\end{cases}, \quad [KN\times KN] \quad (28)$$

$$\boldsymbol{F}_{4,4} = E\left\{\left|\frac{\partial(\cdot)}{\partial\sigma_\eta^2}\right|^2\right\} = \frac{KNM}{{\sigma_\eta^2}^2}, \quad [1\times 1]$$

$$\boldsymbol{F}_{1,2} = \boldsymbol{F}_{2,1}^T = E\left\{\frac{\partial(\cdot)}{\partial\omega_\gamma}\frac{\partial(\cdot)}{\partial\varphi_{k,n}}\right\} = -\frac{\pi}{\lambda\sigma_\eta^2}\frac{MT_a^2}{3}\dot{b}_{k,n}^{\gamma}, \quad [3\times KN]$$

$$\boldsymbol{F}_{1,3} = \boldsymbol{F}_{3,1}^T = E\left\{\frac{\partial(\cdot)}{\partial\omega_\gamma}\frac{\partial(\cdot)}{\partial A_{k,n}}\right\} = 0, \quad [3\times KN]$$

$$\boldsymbol{F}_{1,4} = \boldsymbol{F}_{4,1}^T = E\left\{\frac{\partial(\cdot)}{\partial\omega_\gamma}\frac{\partial(\cdot)}{\partial\sigma_\eta^2}\right\} = 0, \quad [3\times 1]$$

$$\boldsymbol{F}_{2,3} = \boldsymbol{F}_{3,2}^T = E\left\{\frac{\partial(\cdot)}{\partial\varphi_{k,n}}\frac{\partial(\cdot)}{\partial A_{u,l}}\right\} = 0, \quad [KN\times KN]$$

$$\boldsymbol{F}_{2,4} = \boldsymbol{F}_{4,2}^T = E\left\{\frac{\partial(\cdot)}{\partial\varphi_{k,n}}\frac{\partial(\cdot)}{\partial\sigma_\eta^2}\right\} = 0, \quad [KN\times 1]$$

$$\boldsymbol{F}_{3,4} = \boldsymbol{F}_{4,3}^T = E\left\{\frac{\partial(\cdot)}{\partial A_{k,n}}\frac{\partial(\cdot)}{\partial\sigma_\eta^2}\right\} = 0, \quad [KN\times 1]$$

The CRBs for ω_H, ω_R and ω_V are derived by inverting $\boldsymbol{F}$ and reading its elements (1,1), (2,2) and (3,3). By considering the Frobenius relations for partitioned matrices and carrying out the calculus, we found that the bounds correspond to the diagonal elements of a $[3\times 3]$ matrix given by $\left(\boldsymbol{F}_{1,1} - \boldsymbol{F}_{1,2}\boldsymbol{F}_{2,2}^{-1}\boldsymbol{F}_{1,2}^T\right)^{-1}$; carrying out the calculus, we found the diagonal elements (14).

ACKNOWLEDGMENT

This work was partially supported by Selex Galileo CTO - Innovative Projects Analysis & Demonstrations Group (Pomezia, Italy). D. Pastina acknowledges fruitful discussions with Chiara Spina formerly with SELEX-Galileo (now Leonardo).

REFERENCES

[1] D. R. Wehner, *High-resolution radar*. Artech House, Boston, MA, USA, 1992, 2nd edition.

[2] P. Lacomme, J.P. Hardange, J, C. Marchais, E. Normant, *Air and spaceborne radar systems*. William Andrew Publishing, Scitech Publishing Inc, Norwich, NY, USA, 2001, pp. 329–335.

[3] M. Vespe, D. Pastina, C.J. Baker, H.D. Griffiths, P. Lombardo, "Impact of angular processing technique and cross range resolution on 2D radar target classification," *Proc. EUSAR 2006*, Dresden (Germany), May 2006.

[4] M. Vespe, C.J. Baker, H.D. Griffiths, "Automatic target recognition using multi-diversity radar," (2007) *IET Radar, Sonar and Navigation*, 1 (6), pp. 470-478.

[5] S. Musman, D. Kerry, and C. Bachmann, "Automatic Recognition of ISAR Ship Images," *IEEE Trans. Aerosp. Electron. Syst.*, vol. 32, no. 4, pp. 1392-1403, Oct. 1996.

[6] D. Pastina, C. Spina, "Multi-feature based automatic recognition of ship targets in ISAR," *IET Radar, Sonar Navig*., 2009, vol. 3, Issue 4, pp. 406-423.

[7] D. Pastina, C. Spina, "Multi-feature based automatic recognition of ship targets in ISAR images," *2008 IEEE Radar Conference*, Rome (Italy), May 2008.

[8] D. Pastina, C. Spina, "Multi-frame data fusion techniques for ATR of ship targets from multiple ISAR images," *Proc. EURAD 2009*, Rome (Italy), Oct. 2009.

[9] E. Giusti, M. Martorella, and A. Capria, "Polarimetrically-Persistent-Scatterer-Based Automatic Target Recognition," *IEEE Trans. Geosci. Remote Sens.,* vol. 49, no. 11, pp. 4588-4599, Nov. 2011.

[10] G. Wang, X.-G. Xia, and V.C. Chen, "Three-dimensional ISAR imaging of maneuvering targets using three receivers," *IEEE Trans. Image Process*., vol. 10, no. 3, pp. 436-447, Mar. 2001.

[11] X. Xu, R.M. Narayanan, R.M., "Three-dimensional interferometric ISAR imaging for target scattering diagnosis and modeling," *IEEE Trans. Image Process*., vol. 10, no. 7, Jul. 2001, pp. 1094-1102.

[12] Q. Zhang, T.S. Yeo, "Three-dimensional SAR imaging of a ground moving target using the InISAR technique," *IEEE Trans. Geosci. Remote Sens.*, vol. 42, no. 9, Sept. 2004, pp. 1818-1828.

[13] Q. Zhang, T.S. Yeo, G. Du, and S. Zhang, "Estimation of three-dimensional motion parameters in interferometric ISAR imaging," *IEEE Trans. Geosci. Remote Sens.*, vol. 42, no. 2, pp. 292-300, Feb. 2004.

[14] C. Ma, T.S. Yeo, Q. Zhang, H.S. Tan, and J. Wang, "Three-dimensional ISAR imaging based on antenna array," *IEEE Trans. Geosci. Remote Sens.*, vol. 46, no. 2, pp. 504-515, Feb. 2008.

[15] C. Ma, T.S. Yeo, Y. Zhao, J. Feng, "MIMO Radar 3D Imaging Based on Combined Amplitude and Total Variation Cost Function With Sequential

Order One Negative Exponential Form," *IEEE Trans. Image Process*., vol. 23, no. 5, May 2014, pp2168-2183.
[16] M. Martorella, D. Staglianò, F. Salvetti, N. Battisti, "3D interferometric ISAR imaging of noncooperative targets", *IEEE Trans. Aerosp. Electron. Syst.*, vol. 50, no. 4, pp. 3102-3114, Oct. 2014.
[17] D. Pastina, M. Bucciarelli, and P. Lombardo, "Multistatic and MIMO distributed ISAR for enhanced cross-range resolution of rotating targets," *IEEE Trans. Geosci. Remote Sens*., vol. 48, no. 8, pp. 3300-317, Aug. 2010.
[18] M. Bucciarelli and D. Pastina, "Multi-grazing ISAR for side-view imaging with improve cross-range resolution," *Proc. of 2011 Radar Conference*, Kansas City (MO, USA), May 2011.
[19] M. Bucciarelli, D. Pastina, "Distributed ISAR focusing for targets undergoing 3D motion," *IET International Conference on Radar Systems*, Glasgow (U.K.), Oct. 2012.
[20] Y. Zhu, Y. Su, W. Yu, "An ISAR Imaging Method Based on MIMO Technique," *IEEE Trans. Geosci. Remote Sens*., vol. 48, no. 8, Aug. 2010, pp. 3290-3299.
[21] D. Pastina, F. Santi, M. Bucciarelli, "MIMO distributed imaging of rotating targets for improved 2-D resolution," *IEEE Geosci. Remote Sens. Lett*., vol. 12, no. 1, Jan. 2015, pp. 190-194.
[22] AW Doerry, "Ship dynamics for maritime ISAR imaging," SANDIA Report: SAND2008-1020, Feb. 2008.
[23] Z. She and Z. Zhu, "Cross-range scaling of inverse synthetic aperture radar," *Proc. of IEEE NAECON*, Dayton (OH, USA), 1994, pp. 175-180.
[24] A. Jain, "Method and apparatus for determining a cross-range scale factor in inverse synthetic aperture radar," U.S. Patent 5164730 A, 17 Nov. 1992.
[25] J. Sheng, M. Xing, L. Zhang, M.Q. Mehmood, and L. Yang, "ISAR cross-range scaling by using sharpness maximization," *IEEE Geosci. Remote Sens. Lett*., vol. 12, no. 1, Jan. 2015, pp. 165-169.
[26] C.-M. Yeh, J. Xu, Y.-N. Peng, and X.-T. Wang, "Cross-range scaling for ISAR based on image rotation correlation," *IEEE Geosci. Remote Sens. Lett.*, vol. 6, no. 3, July 2009, pp. 597-601.
[27] C.-M. Yeh, J. Xu, Y.-N. Peng, X.-G. Xia, and X.-T. Wang, "Rotational motion estimation for ISAR via triangle pose difference on two range-Doppler images," *IET Radar Sonar Navig*., 2010, Vol. 4, Iss. 4, pp. 528-536.
[28] S.-H. Park, H.-T. Kim, and K.-T. Kim, "Cross-range scaling algorithm for ISAR images using 2-D Fourier Transform and Polar Mapping," *IEEE Trans. Geosci. Remote Sens*., vol. 49, no. 2, Feb. 2011, pp. 868-877.
[29] S.-B. Peng, J. Xu, Y.-N. Peng, J.-B. Xiang, X.-G. Xia, Inverse synthetic aperture radar rotation velocity estimation based on phase slope difference of two prominent scatterers," *IET Radar Sonar Navig*., 2011, Vol. 5, Iss. 9, pp. 1002-1009.
[30] C.-M. Yeh, J. Xu, Y.-N Peng, X.-T. Wang, J. Yang, "Cross-Range Scaling for ISAR via Optical Flow Analysis," *IEEE Aerosp. Electron. Syst. Mag*, vol. 27, no. 2, pp.14-22, Feb. 2012.
[31] J. Xu, X.-G. Xia, S.-B. Peng, J. Yu, Y.-N. Peng, L.-C. Quian, "Radar Maneouvering Target Motion Estimation Based on Generalized Radon-Fourier Transform," *IEEE Trans. Signal Process*., vol. 60, no. 12, pp. 6190-6201, Dec. 2012
[32] D. Pastina, "Rotation motion estimation for high resolution ISAR and hybrid SAR/ISAR target imaging," *Proc. of IEEE 2008 Radar Conference*, Rome (Italy), May 2008.
[33] M. Martorella, "Novel approach for ISAR image cross-range scaling," *IEEE Trans. Aerosp. Electron. Syst.*, vol. 44, no. 1, pp. 281-294, Jan. 2008.
[34] Y. Wang, Y. Jiang, "A Novel Algorithm for Estimating the Rotation Angle in ISAR Imaging," *IEEE Geosci. Remote Sens. Lett*., vol. 5, no. 4, pp.608-609, Oct. 2008.
[35] V.C. Chen, W.J. Miceli, "Simulation of ISAR imaging of moving targets," *IEE Proc. Radar, Sonar Navig*., vol. 148, no. 3, June 2001.
[36] D. Pastina and C. Spina, "Slope-based frame selection and scaling technique for ship ISAR imaging," *IET Signal Process*., vol. 2, Issue 3, pp. 265-276, Sep. 2008.
[37] S. Brisken, M. Martorella, "Multistatic ISAR autofocus with an image entropy-based technique," *IEEE Aerosp. Electron. Syst. Mag*, Vol. 29, Issue 7, 2014, pp. 30-36.
[38] C.-M. Yeh, J. Xu, Y.-N. X.-T Wang, "ISAR image fusion with two separated aspect observation," *Proc. of IEEE Radar Conf*., May 2009.
[39] D. Pastina, M. Bucciarelli, C. Spina, "Multi-sensor rotation motion estimation for distributed ISAR imaging," *Proc. of the 6th European Radar Conference*, Rome (Italy), Oct. 2009.
[40] F. Santi, M. Bucciarelli, D. Pastina, "Target rotation motion estimation from distributed ISAR data," *Proc. of IEEE 2012 Radar Conference*, Atlanta (GA, USA), May 2012.
[41] F. Santi, D. Pastina, M. Bucciarelli, "Multi-sensor ISAR techniques for motion estimation of pitching, rolling and yawing targets," *Proc. of IEEE 2013 Radar Conference*, Ottawa (Canada), May 2013.
[42] S. Barbarossa, "Detection and imaging of moving objects with SAR – Part I: optimal detection and parameter estimation," *IEE Proc. on RSN*, vol. 138, no. 2, 1992, pp. 79-87.
[43] X. Xu, L. Zhai, and Y. Huang, "Subpixel processing for target scattering center extraction from SAR images," *8th International Conference on Signal Processing*, vol.4, 2006.
[44] J.T. Mayhan, M.L. Burrows, K.M. Cuomo, J.E. Piou, "High resolution 3D 'snapshot' ISAR imaging and 3D feature extraction," *IEEE Trans. Aerosp. Electron. Syst.*, vol. 37, no. 2, Apr. 2011, pp. 630-641.
[45] M. Skolnik, *Radar Handbook*, 3rd ed. New York: McGraw-Hill, 2008, pp. 23.19–23.20.
[46] Dan E. Dudgeon, Richard T. Lacoss, Carol H. Lazott, Jacques G. Verly, "Use of persistent scatterers for model-based recognition," *Proc. SPIE 2230, Algorithms for Synthetic Aperture Radar Imagery*, 356 (June 9, 1994).
[47] H. Wu, D. Grtenier, G. Y. Delisle, and D.-G. Fang, "Translational motion compensation in ISAR image processing," *IEEE Trans. Aerosp. Electron. Syst.*, vol. 32, no. 3, pp. 1191-1197, Jul. 1996.
[48] B. Ristic, B. Boashash, "Comments on 'The Cramer-Rao Lower Bounds for Signals with Constant Amplitude and Polynomial Phase'," *IEEE Trans. on Signal Processing*, vol. 46, no. 6, pp. 1708-1709, Jun. 1998.
[49] N. Levanon, *Radar principles*. John Wiley & Sons, 1988.
[50] D. Pastina, F. Santi, M. Bucciarelli, "Multi-angle distributed ISAR with stepped-frequency waveform for surveillance and recognition," *Proc. of 2011 IEE CIE International Conference on Radar*, vol. 1, pp. 528-532, Oct. 2011
[51] S. Kay, *Fundamentals of Statistical Signal Processing*. Englewood Cliffs, NJ: Prentice-Hall, 1993.

Fabrizio Santi was born in Rome, Italy, in July 1985. He received the Master's degree (*cum laude*) in telecommunication engineering and the Ph.D. degree in remote sensing from Sapienza University of Rome, Rome, Italy, in September 2010 and June 2014, respectively.

From April to September 2013 he carried on research activity with the Microwave Integrated Systems Laboratory, University of Birmingham, Birmingham, U.K. He is currently a Postdoctoral Researcher with the Department of Information Engineering, Electronics and Telecommunications (DIET), Sapienza University of Rome. The results of his research activity have been reported in a number of journals and conference papers. His main research interests include multisensor SAR/ISAR radar imaging and space-based passive radar.

Dr. Santi frequently serves as a Reviewer for the IEEE JOURNAL OF SELECTED TOPICS IN APPLIED EARTH OBSERVATION AND REMOTE SENSING, the IEEE TRANSACTION ON AEROSPACE AND ELECTRONIC SYSTEMS, and other international technical journals. He received the Best Italian Thesis on Remote Sensing Award from the IEEE Geoscience and Remote Sensing South Italy Chapter in 2010.

Debora Pastina (M'01) received the Laurea degree in telecommunications engineering and the Ph.D. degree in information and telecommunications engineering from Sapienza University of Rome, Rome, Italy, in 1996 and 2000, respectively, respectively.

From July 1998 to March 1999, she carried on research activity with the SAR Processing Team, Defence Evaluation Research Agency (DERA), Malvern, U.K. She is currently an Assistant Professor with the Department of Information Engineering, Electronics and Telecommunications (DIET), Sapienza University of Rome, where she teaches different courses in remote sensing and telecommunication. She is involved and is responsible of scientific research

projects funded by the Italian Ministry of Research, by the Italian Space Agency, by the European Commission and by the national radar industry. The results of her research activity have been reported in a number of journal and conference papers. Her main research interests include SAR/ISAR signal processing, ground moving target indication techniques, GNSS-based passive radar systems, clutter models, coherent and incoherent radar detection in non-Gaussian clutter and CFAR radar techniques.
Dr. Pastina was the Chairman of the Local Committee of the IEEE/ISPRS Joint Workshop on Remote Sensing and Data Fusion over Urban Areas (Rome, November 2001). She was the Publication Chair of the 2008 IEEE Radar Conference held in Rome in May 2008. She has been a member of the Editorial Board of the International Journal of Electronics and Communications (AEÜ, Elsevier) acting as Area Editor for radar systems and techniques since September 2012. She serves as Associate Editor for Radar Systems for the IEEE Transactions on Aerospace and Electronic Systems since May 2017. She has served in the technical review committee of many international conferences on radar systems and remote sensing. From many years, she has served as a Reviewer for a number of international technical journals.

Marta Bucciarelli was born in Rome, Italy, in May 1981. She received the Laurea degree in communication engineering and the Ph.D. in radar and remote sensing from Sapienza University of Rome, Rome, Italy, in 2006 and 2010, respectively. In 2010, she received a four-years research contract on "Signal Elaboration techniques for mono or multistatic radars with long coherent integration time" at the DIET department (University of Rome "La Sapienza"). In 2014, she joined the NATO STO Centre for Maritime Research and Experimentation as a Visiting researcher working on an experimental X-band Radar Sensor Network for distributed imaging of ship targets. She works for the academic spinoff Sympas S.r.l, which she co-founded in 2009. She has been and is involved in scientific research projects funded by the European Commission (FP7 and H2020), the Italian Space Agency, the Italian Ministry of Research and the Italian industry. Her research has been reported in a number of publications conference proceedings. In addition to her research activities, she has undertaken teaching activities since 2010 for the course "Radar and Remote sensing" (degree in Information Engineering - Latina) and since 2012 for the courses of "Telecommunication and Radar Earth Observation" of the Master' degree in Satellite Systems and Services (Sapienza University of Rome). Moreover, she has been involved as tutor in several courses, such as "Air Traffic Control", "Radar Imaging Elaboration", "Radar and Remote Sensing laboratory course", "Basic Telecommunications and remote Sensing", and "Radar Systems". Her current research interests include multi-channel active, passive, multistatic and MIMO high-resolution ISAR imaging, adaptive multi-channel signal processing for beamforming and interference cancellation, space surface passive bistatic and multistatic SAR imaging and detection of maritime targets using GNSS transmitters of opportunity.

Dr. Bucciarelli serves as a Reviewer for international journals, conferences, and scientific books.